Addis Ababa University

Addis Ababa Institute of Technology

Center of Biomedical Engineering

Characterization of Antibubbles Response under Sonication In Terms of Size Distribution and Destruction Threshold for Use in Drug Delivery

A Thesis Submitted to Center of Biomedical Engineering

In Partial Fulfillment of the Requirements for the Degree of Master of Science

In Biomedical Engineering

(Bioinstrumentation and Imaging)

By: Mahider Yifru Addisu

Advisor: Dawit Assefa Haile (PhD)

Co-Advisor: Michiel Postema (PhD)

Addis Ababa, Ethiopia

Declaration

I, Mahider Yifru, declare that this thesis entitled “Characterization of Antibubbles Response under Sonication In Terms of Size Distribution and Destruction Threshold for Use in Drug Delivery” and the work presented in it are my own. I confirm that:

- This work was done wholly or mainly while in candidature for M.Sc. degree at this University.
- This thesis has not previously been submitted for a degree or any other qualification at this University or any other institution.
- Where I have consulted the published work of others, this is always clearly attributed.
- Where I have quoted from the work of others, the source is always given. With the exception of such quotations, this thesis is entirely my own work.
- I have acknowledged or cited all the main sources of help.

Signed:

_____

Date:

_____

I, Dawit Assefa Haile (PhD), certify that the thesis submitted is done under my supervision and sufficiently well prepared for examination.

Signed:

_____

Date:

_____

Certificate of Examination

This is to certify that the thesis prepared by Mahider Yifru Addisu entitled: *Characterization of Antibubbles Response under Sonication In Terms of Size Distribution and Destruction Threshold for Use in Drug Delivery* submitted in partial fulfillment of the requirements for the degree of Master of Science in Biomedical Engineering (Bioinstrumentation and Imaging) complies with the regulations of the University and meets the accepted standards with respect to originality and quality.

Signed by the examining committee

Examiner: _____ Signature _____ Date: _____

Examiner _____Signature _____ Date: _____

Examiner _____Signature _____ Date: _____

Examiner _____Signature _____ Date: _____

_____

Chief of department or Graduate program coordination

Abstract

Antibubbles are gas bubbles containing liquid droplets. Due to their acoustic property, they are preferable for different medical applications such as drug delivery and ultrasonic harmonic imaging. In drug delivery, they are used as drug carrier for effective treatment of diseases such as cancer. In order to ensure safe and targeted drug delivery, the behaviors of the drug carriers (antibubbles) need to be studied. The aim of the current research was to study response of antibubbles under sonication and determine destruction threshold which can lead to fragmentation under ultrasound pulse having safe mechanical index (MI) with reduced undesired mechanical and thermal bio-effects. Gray-scale video frames of antibubbles were used for this research, which were generated through laboratory experiment. Matlab and ImageJ platforms were used for effective detection of antibubbles and determination of their respective size before, during and after sonication together with destruction threshold. The proposed algorithm involves extraction of texture features form the video frames based on the local gray level co-occurrence matrix (GLCM) and a watershed scheme for segmentation of the antibubbles. Once antibubbles are detected, their size distribution under ultrasound pulse with varying acoustic pressures was analyzed. The investigation carried out under sonication of low pressure ultrasound waves (0.2 MPa and 0.4 MPa) showed that the antibubbles oscillate repeatedly with series of stable contraction and expansion but will not undergo fragmentation. This property of antibubbles interaction with low pressure ultrasound wave makes them very useful and preferable to be used as a drug carrier in a way of manipulating the antibubble movement through the blood vessel to the target region. In case of antibubble sonication under higher acoustic pressure wave (0.6 MPa and 1 MPa), their oscillations become more asymmetric which finally lead to fragmentation. The MI of 0.6 MPa and 1Mpa ultrasound pulses are 0.6 and 1 respectively, where significant risk of cavitation is considered for MI > 0.7. The destruction threshold analysis showed that antibubbles under acoustic pressure of 0.6 MPa experience fragmentation when their size during maximum expansion is approximately twice that of their initial size intermes of area, i.e. $A_{max} \approx 2.1\ A_{i.}$ In the case of 1 MPa acoustic pressure $A_{max} \approx 2.8\ A_i$, showing that ultrasound pulse with acoustic pressure of 0.6 MPa is considered safe compared to 1 MPa for use in drug delivery with the capacity to induce fragmentation and effective targeted drug release.

Keywords: antibubble, acoustic pressure, drug delivery, GLCM, sonication, ultrasound, watershed.

Acknowledgment

First and foremost, thanks to God for being with me throughout the path and letting me finish this thesis. Second I would like to express my deepest gratitude to my thesis advisor, Dr. Dawit Assefa. He is the one who has created a relation with external biomedical expert, Prof. Michal Postema, and got the project problem and the necessary resources. Third, I would like to thank my co-supervisor, Prof. Postema for providing the necessary experimental data and all supporting comments. Last but not least, I would like to thank my families and Biniyam Ahmed for the unconditional support and care.

Table of Content

List of Figures

List of Tables

List of Abbreviations

ANN	Artificial Neural Network
CLAHE	Contrast Limited Adaptive Histogram Equalization
Fc	Center Frequency
FDA	Food and Drug Administration
GLCM	Gray Level Co-Occurrence Matrix
HIFU	High Intensity Focused Ultrasound
MI	Mechanical Index
MRGFUS	Magnetic Resonance Guided Focused Ultrasound
MRI	Magnetic Resonance Imaging
PDE	Partial Differential Equation
PNP	Peak Negative Pressure
PPP	Peak Positive Pressure
P2P	Peak-to-Peak Pressure
PRT	Pulse Repetition Period
PRF	Pulse Repetition Frequency

Chapter 1: Introduction

1.1 Background

Drug delivery is the method or process by which a drug is administered into the body of humans or animals for therapeutic purposes [1]. Many researches have been done to come up with better drug delivery mechanism to ensure effective therapy and bioavailability of the drug at the target area with the right dosage. Minimizing toxicity to non-targeted region is the major need for efficient drug delivery that is influenced by the penetration of the drug before reaching the right target. For example, during cancer treatment, there are several physical barriers that limit the penetration of the drug and affect its transportation along the path to the target. Different approaches have been studied to solve this problem by maximizing the drug localization to reach the target and minimizing toxicity to non-targeted regions.

Recently, controlled and targeted drug delivery is gaining more attention [2]. Biocompatibility and formulations of the drug carrier to fit the physicochemical properties of the drug are the major pre-requisites for their pharmaceutical use [1]. Use of microbubbles (gas bubbles in microns) and antibubbles is one of the major advancements under investigation in the area of drug carrier manufacturing which has been important to the development of new therapeutics containing both hydrophilic and hydrophobic drugs entrapped within the core droplet or the gaseous/liquid shell. The purpose of using these carriers is to obtain a controlled and targeted release thus maintaining accurate dosage and timing while reducing side effects related to drug exposure of the non-targeted healthy environment. This concept has significant role in areas such as oncology (the study and treatment of tumors) since side effects from chemotherapeutic drugs with narrow therapeutic window (range between their effectiveness and toxicity) can limit the dose and compromise effectiveness of the treatment [3].

In targeted drug delivery, the drug is transported from the site of administration to specific targeted site (diseased tissue or tumor) guided by imaging modalities such as MRI and ultrasound. Imaging is used to identify target and non-target anatomy, screening, planning, monitoring, and post procedural assessment of treatment outcomes. One of the most recent approaches in this area is “Ultrasound-guided and targeted drug delivery” which uses ultrasound to facilitate better customization of targeted drug delivery [4]. The use of ultrasound is attractive

and preferable due to its peculiar advantages [5]. The main advantages include availability, accurate focus to deeply seated organs, non-invasiveness, non-viral and non-ionizing nature, and their low cost.

In addition the ultrasound induced physiological effect is the basic concept behind this ultrasound guided and triggered drug delivery approach using drug carrier, which is the process of sonoporation (see Figure 1.1) [4] [6]. In this process pore formation happens in walls of blood vessels which allow the drug to penetrate and reach the target region. Pore formation happens due to physical effect such as sheer stress, micro-streaming and shock wave as the result of ultrasound induced cavitation of the drug carrier.

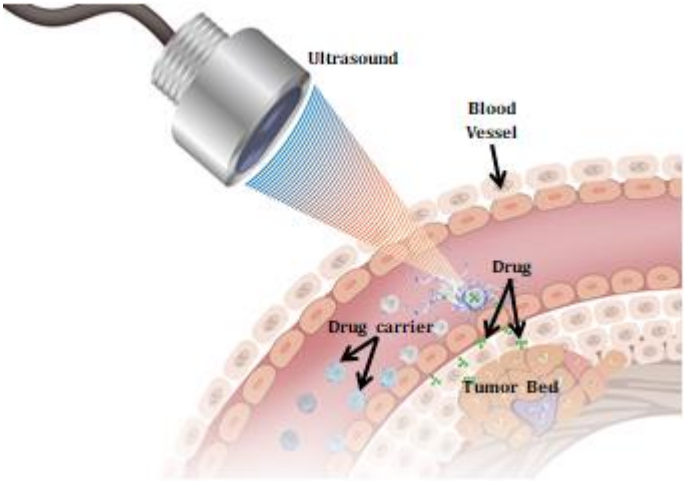

Figure 1.1 Ultrasound-guided local drug delivery using drug carriers [6].

The interaction of these drug carriers with ultrasound is known as “acoustic cavitation” and it can be of two types [7]. The first one is stable cavitation which allows oscillation of the antibubbles through the blood vessel without collapse and it occurs at low acoustic amplitudes. The second type is inertial cavitation, which causes drug release by making the antibubbles to fragment once it reaches the target site and it occurs relatively at higher acoustic amplitudes.

The use of ultrasound in drug delivery is highly influenced by the development of drug carriers such as microbubbles and antibubbles. Based on the literatures, for such kind of therapeutic applications, use of microbubbles can generate three basic responses to ultrasound wave [6]. The first response is the one we see at low acoustic amplitudes which are used for imaging purposes (guiding) with Mechanical index (MI) < 0.2. In this case microbubbles show vibration causing small rupture of cell membranes locally but have limited ability for regional drug delivery. The

second response happens when increasing the acoustic amplitude microbubbles (MI between 0.2 and 0.8). Here microbubbles show stable oscillations which become more asymmetric with increasing pulse amplitude while limited microbubble disruption begins to emit low-energy shock waves. This causes changes in vascular permeability which allows local drug uptake, as a result of large rapture in capillaries, a phenomenon termed as sonoporation. The third response is when the acoustic amplitude is increased further (MI > 0.8) and microbubbles show inertial cavitation emanating high-energy shock waves, which also results in fragmentation and drug release from the drug carrier. But the high- energy shock waves might cause some unwanted bio-effects. In general, the use of ultrasound wave in target drug delivery results in microbubbles oscillation inside the microcirculation path, increases local permeability of the vasculature, and allows drug release at the target region.

Various researches have been done on physics and behavior of bubbles, and acoustics–bubble interactions as well. In the year 2005, research was done on ultrasonic fragmentation of microbubbles using a theoretical approach [8]. The paper investigated how microbubbles collapse and fragment. It used theoretical approach on fragmentation followed by experiments and high speed optical observations to study collapse and fragmentation of microbubbles under sonication. For the experiment, lipid-encapsulated microbubbles were used and high speed photographic image data were taken in different frames before and during sonication. It was also hypothesized that fragmentation will occur if and only if the instantaneous bubble surface energy is less than the kinetic energy of the collapsing microbubbles, which will induce surface instabilities. The work generally tried to investigate fragmentation of the microbubbles (used as ultrasound contrast agents) with respect to its kinetic energy.

In 2007, another research was done on ultrasonic bubbles and influence of their shells up on sonication [9]. The research explored the behavior of microbubbles when they are subjected to an ultrasound pulse, with special attention to the influence of the bubble shell. When a bubble is under sonication, it encounters higher harmonic oscillations. For encapsulated microbubbles, the shells have a great effect on their interaction with ultrasound. For the simulation work, Matlab was used with different parameters of the microbubbles such as surface tension, viscosity and stiffness of the shell. Similarly, different ultrasound wave parameters such as amplitude and frequency were used. The simulation result showed that microbubbles fragmentation and ultrasonic cracking are disruptive phenomena that are usually observed in high acoustic

amplitudes. The study also analyzed the occurrence of microbubbles fragmentation by simulating the oscillating behavior of encapsulated microbubbles with various sizes in a harmonic acoustic field. Similar to the research done in 2005, this paper concluded that fragmentation occurs exclusively during the collapse phase of the bubbles when the instantaneous bubble surface energy is less than the kinetic energy of the collapsing microbubbles. This as a result makes the surface instabilities to grow big enough to allow the break-up.

The primary drawback of using microbubbles compared to antibubble is that most of their content is gas, rather than drug or gene payload, which makes the amount of drug that can be administered into the shell very limited [6] [10]. In addition, drug loading in micro-bubble's shell affects biological activity of the drug and its acoustic response. It is often difficult for drugs to release from shell of the microbubble. Furthermore, microbubbles are less stable in circulation compared to antibubbles. Various drug carriers have been investigated to solve this issue with combination of gases (i.e., air, oxygen and sulfur hexafluoride) and liquid (i.e. phospholipids, surfactants, proteins, and synthetic polymers). In such a way antibubbles are developed as an alternative and preferable drug carrier. Main reason that makes antibubbles to be preferable for drug delivery is that their liquid droplet cores can be replaced by therapeutic agents. Figure 1.2 presents a typical picture of antibubbles under a microscope taken using a high speed photography camera before sonication (the application of ultrasound pulse on particles).

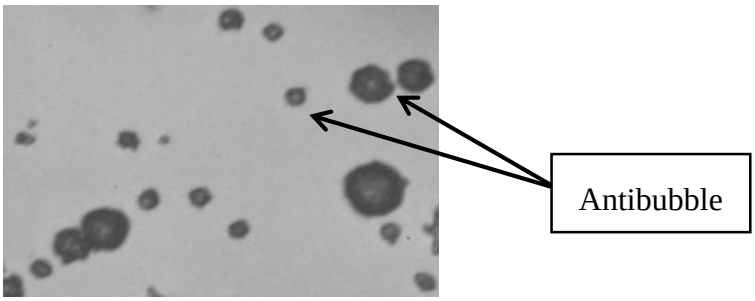

Figure 1.2 Antibubbles taken using high speed photography camera before sonication.

In 2007, a study found out that incorporating liquid droplets inside the bubble, termed as antibubble, would be interesting in order to solve the problems related to microbubbles [11]. One other issue with antibubbles is their lifetime which often in the order of minutes. Two research findings were reported in the years 2011 and 2013 that suggested mechanisms for the productions of better antibubbles with increased life time [12] [13].

Though several studies are reported on antibubbles, however, only few dealt with their interaction with ultrasound. In 2015, two studies were conducted on acoustically active antibubbles [14] [15]. The studies analyzed the behavior of antibubbles when subjected to an ultrasonic pulse. In the first study, an oscillating behavior of antibubbles under sonication was derived, resulting in a Rayleigh-Plesset equation of antibubble dynamics with the assumption that antibubbles are made having negligible outer shell [14]. The second study compared behavior of antibubbles with regular gas bubbles [15]. The results showed that if the antibubble's liquid core radius is less than half the antibubble's radius, both antibubbles and regular bubbles respond in a very similar manner when they are under sonication. But antibubbles with larger cores show higher harmonic behavior, which would make them preferable for use in ultrasonic harmonic imaging and also for drug delivery.

Another study was conducted in 2018 on harmonic response of microscopic antibubbles [16]. The study followed an experimental approach by using prefabricated antibubbles and identical bubbles without core droplets subjected to ultrasound wave with different parameters. Then the spectra were recorded with a broadband transducer which is placed perpendicularly to the transmitter. The data was then normalized by the acoustic response from the medium and as a result the antibubble signal shows stronger harmonics than the signal produced by the regular bubbles. Based on the results, the study concluded that antibubbles are advantageous for use in harmonic imaging and also in drug delivery.

In one of the recent works done in 2019, a research was carried out on how to control the lifetime of antibubbles [17]. The study was governed by the fundamental theory that the lifetime of antibubbles depends on the electrical potential between the two liquid-gas interfaces. The paper mainly investigated the effects of surface elasticity in antibubbles lifetime. The study also investigated other effects such as influence of under-saturated liquid with air and influence of dust particles on antibubble stability. It followed experimental approach with a new antibubble generator and independent surface elasticity measurements. Then it concluded that it is possible to control the lifetime of antibubbles and also clarified the effects of antibubbles' radius on their lifetime together with the role of surface rheology.

So far attempts to determine destruction threshold of microbubbles under ultrasonic pulses were done, mostly based on theoretical approaches with the use of experiments as confirmation but

less is done for antibubbles. One MSc dissertation done by Nicole Anderton at the University of the Witwatersrand, Johannesburg, South Africa focused on acoustic properties of antibubbles [18]. The study explored the stability, predictability and other acoustic properties of antibubbles in comparison with regular gas bubbles. Analysis of the size distribution of the antibubbles was preceded by their detection. The study found out those oscillations of antibubbles is more asymmetric than that of regular bubbles since antibubbles have incompressible liquid cores which restrict their contraction and expansion. In addition, antibubbles are more stable and predictable under the influence of ultrasound than regular bubbles that are currently used in drug delivery. The study also showed that a single pulse of ultrasound, with a peak negative pressure of 1 MPa, was enough to destruct all the antibubbles and release their content. It is known that ultrasound pulse with high MI > 0.7 causes larger inertial cavitation with high risk of unwanted bio-effects. The study exploited image processing techniques making use of a simple gray-level-window slicing technique together with Otsu's thresholding to detect antibubbles observed in photographic images generated experimentally. In instances where the thresholding method failed, a manual technique was employed to obtain the threshold values, which made identification of the exact boundaries of the antibubbles difficult.

In this regard, developing a more effective and fully automated antibubble detection algorithm could have vital importance in the subsequent size determination of the antibubbles and computing their destruction thresholds when they are under sonication. Such algorithm should also account for detection of antibubbles that might overlap during sonication. In general, for effective drug delivery applications, size distribution of the antibubbles and their dynamic behavior under sonication needs to be predicted in greater details, with a focus on destruction threshold of their inertial cavitation due to acoustic wave of specific parameters. Such and similar issues need to be resolved before antibubbles are used for effective drug delivery applications, diagnostic imaging and their variants.

The most recent work on antibubbles was published in April, 2022 with the aim of testing drug loading antibubbles in vivo experiment, which showed that antibubbles do not have any acute toxicity after injection based on an animal study [19]. It also proved that use of antibubbles is a viable concept for ultrasound guided drug delivery with better drug loading and stability allowing their fragmentation and subsequent drug release under safer MI.

1.2 Statement of the Problem

Use of antibubbles as a drug carrier is one of the most recent advancements for effective drug delivery while reducing side effects related to the exposure of non-targeted regions to the active agent (drug) [6] [14]. In addition, when the drug is transported through cells and tissues, it faces different physiological barriers before reaching the target which will affect the effectiveness of the drug delivery [20] [21]. Encapsulating drugs within micron sized antibubbles is suggested to ensure targeted delivery mechanism allowing release of sufficiently high concentrations of the drug only when it reaches the target which is done exploiting ultrasound pulses [4]. For this to be achieved, the properties of the drug carrier should be studied carefully including its interaction with ultrasound pulses. Based on the literature review several studies are reported on antibubbles in general and their potential to be used as a drug carrier, but only few dealt with their interaction with ultrasound. In addition the existing theories need a proof of concept by experimental analysis. Safety is also one of the greatest requirements during this process since the cavitation phenomenon might cause harmful bio-effects (thermal and mechanical) if it is out of the allowed MI range. Therefore, it is essential to characterize antibubbles under sonication intermes of their size distribution and destruction threshold, which is applicable and useful in design and production of the antibubbles to be used as drug carriers within safe MI range.

1.3 Objectives

1.3.1 General Objective

The general objective of the current research is characterizing antibubbles under sonication, quantification of their size distribution and determination of their destruction threshold.

1.3.2 Specific Objectives

- Detect antibubbles in a given photographic image.
- Determine actual size of the antibubbles based on image processing.
- Obtained and analyze the size distribution of antibubbles under different ultrasonic pressures.
- Study antibubble interaction with ultrasound.
- Determine the fragmentation threshold.

1.4 Significance of the Thesis

The use of antibubbles as a drug carrier for therapeutic purposes is one of the biggest advancements in areas of drug delivery. The main intent of the current thesis work is characterization of antibubbles including their size distribution and destruction threshold. This will play crucial role in ensuring controlled and safe manipulation of the drug. Determining the size of the antibubbles at different phases (before, during, and after sonication) is significant in order to be able to investigate effect of ultrasound pulse on antibubbles to ensure safe and efficient drug delivery. The determination of the destruction threshold is important to reduce unwanted bio-effects and make sure the acoustic parameters are within clinically safe range.

1.5 Scope of the Thesis

This thesis work focuses on the determination of the actual size distribution of antibubbles under different acoustic amplitudes and determining their destruction threshold during inertial cavitation. The investigation involves detecting antibubbles from given experimental video footages taken under a microscope with high speed photography. The size determination is preceded by accurate segmentation of the antibubbles. Then destruction threshold of the antibubbles under sonication is determined. The destruction threshold is calculated in terms of maximum area of expansion the antibubbles just before they fragment. The effect of the core size and the number of droplets inside the antibubbles is not considered in the current study and is beyond its scope.

1.6 Organization of the Thesis

This rest of the thesis has been organized into five chapters. C**hapter 2** defines the theoretical concepts in two basic parts, part one focuses on ultrasound wave and its application in drug delivery. While part two explains about antibubbles, their structure and composition, the drug loading mechanism, requirements to be used as drug carrier, and ultrasonic response of antibubbles **Chapter 3** includes the material and methodology utilized in the proposed antibubble characterization scheme using experimental approach including the different stages of the image processing algorithm together with the post processing and analysis steps. **Chapter 4** presents the results and useful discussion while **Chapter 5** concludes the study incorporating commendations and possible future directions.

Chapter 2: Theoretical Consideration

2.1 Ultrasound and its Applications

Ultrasound waves are acoustic waves (longitudinal waves that are generated by means of vibration) that propagate through matter with a frequency above 20 KHz [22]. They are also known as ultrasonic and human ear cannot hear these acoustic signals. The audible range for acoustic wave is 20 Hz - 20 KHz which is called sound wave. The acoustic wave with a frequency below 20 KHz is also not audible and known as infrasonic or infrasound. For many years, ultrasound has been employed in medicine for therapeutic purposes in addition to diagnosis. The very first therapeutic application of ultrasound wave was discovered in 1930s for tissue heating and healing [23]. Following that, in 1940s, focused ultrasound was studied to be used as an alternative for tissue ablation. Similarly, different researches were carried out to use ultrasound for therapeutic applications such as physiotherapy, neurosurgery, cancer treatment, lithotripsy (mechanical destruction of kidney stones), cataract treatment, acoustic targeted drug delivery and lipectomy. One of the recent advancements of ultrasound wave in therapeutic areas is drug delivery, that includes high-intensity focused ultrasound (HIFU) and magnetic resonance guided focused ultrasound (MRgFUS) drug delivery for soft tissue cancer treatment using drug carriers such as antibubbles.

2.1.1 Principles of Medical Ultrasound

It is important to understand the basic principles of ultrasound in order to have better understanding regarding the bio-effects and safety issues related to its medical applications. Ultrasound is a type of acoustic wave that propagates in a medium in longitudinal direction. It is generated by a transducer using a piezoelectric element and can be focused since it is transmitted in a straight line fashion [24]. The generated ultrasound pulses by the transducer are applied to tissues and reflected echoes are collected back by the transducer. The transducer converts electrical energy to sound energy and vice versa. When an ultrasound pulse travels through a tissue, its amplitude gets reduced (attenuated) due to factors such as absorption, scattering or reflection [23]. The rate of attenuation depends on the tissue type, the frequency of the pulse and the distance it travels throughout the body.

Table 2.1 presents the coefficient of attenuation for ultrasound pulse having frequency of 1MHz in different body tissues measured in decibel per centimeter.

Type of body tissue	Attenuation coefficient (dB/cm at 1 MHz)
Water	0.002
Blood	0.18
Fat	0.63
Liver	0.5-0.94
Kidney	1.0
Muscle	1.3-3.3
Bone	5.0

Table 2.1 Attenuation coefficients of ultrasound pulse at 1MHz frequency in different body tissues [23].

There are different properties that characterize ultrasound waves such as center frequency, dominant period, pulse length, duty cycle, peak negative and positive pressures, peak-to-peak pressure, pulse repetition time and pulse repetition frequency [22]. Figure 2.1 shows the visual representation of these properties for three ultrasound pulses each having three cycles. The center frequency is defined to be the number of oscillations per second while the time required for one cycle is termed as period, which is the reciprocal of the central frequency. The total time taken by the pulse is termed pulse length while duty cycle is the transmission time per each pulse, often written as a percentage [22].

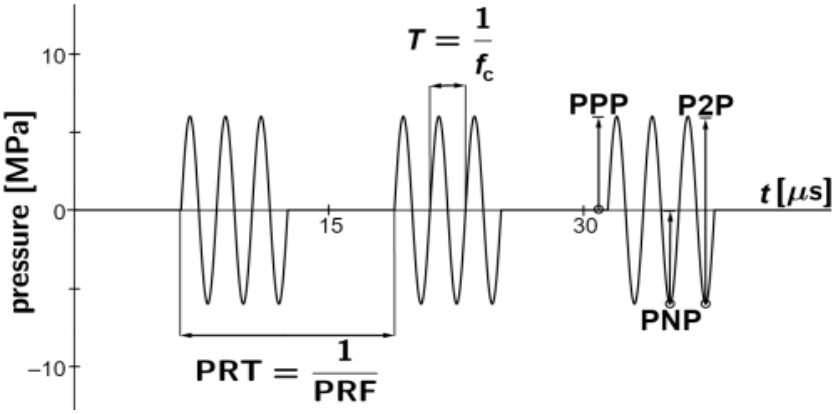

Figure 2.1 Ultrasound pulse representation consisting of three cycles where fc- center frequency, T- dominant period, PPP- peak positive pressure, PNP- peak-negative pressure, P2P- peak-to-peak pressure, PRT- pulse-repetition period and PRF- pulse-repetition frequency [25].

2.1.2 Ultrasound Parameters

Ultrasound parameters play a great role in controlling the process of ultrasound mediated drug delivery using drug carrier such as bubbles and antibubbles. The dynamics and fragmentation of the drug carriers, specifically antibubbles, is highly dependent on the ultrasound parameters such as frequency, intensity, mechanical index and exposure duration [4].

2.1.2.1 Frequency

Depending on the tissue type utilized in preclinical studies, the common ultrasonic frequency employed for drug delivery ranges from kHz to MHz [4]. It is also variable depending on its application. For example, ultrasonic frequency used for therapeutic purposes is lower than that used for diagnosis. This is because low ultrasonic frequencies penetrate deeper which ensures a better therapeutic outcome. The other consideration to select appropriate ultrasonic frequency is the type of drug carrier used since ultrasonic frequency of the wave is somehow related to the resonant frequency of the drug carrier. But the effect of ultrasound frequency is less relevant compared to the acoustic pressure in case of higher acoustic pressure.

2.1.2.2 Intensity

Ultrasound wave intensity determines the amount of energy that is carried by the wave. In drug delivery, it is directly proportional to the acoustic pressure of the wave. Based on the Food and Drug Administration (FDA), ultrasound intensity is regulated to be in a range between 0.3 and 3.0 W/cm^2 for drug delivery applications [4]. This regulation is made to prevent potential tissue damage that can be caused as a result of ultrasound related heating effect. But if the duty cycles are decreased, then it might be possible to use higher ultrasound intensities (taking into consideration the risk of inertial cavitation) since it reduces the temporal average intensity. The duty cycles can be decreased either by reducing the pulse length or by reducing the pulse repetition. The inertial cavitation effect when using high intensity waves is, however, of important concern.

2.1.2.3 Mechanical Index

Mechanical index (MI) is a unit less number that is expressed as a ratio of peak negative pressure to the square root of the center frequency [4]. Since MI is directly proportional to the acoustic pressure applied, it can also be related with ultrasound intensity or used as a substitute. Thus, it is usually used as a direct indicator of the amount of cavitation generated. According to FDA

regulation, the recommended range for MI is usually between 0.2 and 1.9 to avoid unwanted thermal effect during treatment. The upper limit of the MI is set to be 1.9 considering direct tissue damage for clinical applications of ultrasound [4] [26]. But considering also the cavitation effect, based on theoretical study by Apfel and Holland in 1991, the upper bound of MI is chosen to be 0.7 in order to reduce unwanted bio-effects as a result of higher inertial cavitation [22] [27].

2.1.2.4 Duty Cycle (Time Duration)

Time duration of the ultrasound pulse should be considered in order to reduce undesired thermal effects. While using high pressure ultrasound pulse, periodic or persistent injections of drug carriers, as well as longer treatment periods, can improve delivery efficacy, inducing instantaneous inertial cavitation [4]. But high pressures can harm the tissues due to the significant risks of inertial cavitation. In case of lower pressures ultrasound pulses, the time duration should be taken into account for stable oscillation of drug carriers in order to provide optimal drug delivery. This is because even if the pressure is low, prolonged treatment periods can produce heating. Therefore, the duration should be somehow optimized.

2.1.3 Applications of Ultrasound in Drug Delivery

Ultrasound wave is getting highest importance in targeted drug delivery. The process basically relies on the interaction between a biocompatible drug carrier and an acoustic wave. When an antibubble, for example, is subjected to an ultrasound pulse, it causes it to oscillate, generating spherical wave which radiates outwards [28]. Translocation of the antibubble may also occur if there is nearby antibubble that attract or repel it [29]. If the pressure of the ultrasound wave exceeds the cavitation threshold, significant risk of inertial cavitation could be observed. Safety is one of the greatest requirements during this process since this phenomenon might cause harmful bio-effects if the cavitation is out of the allowed mechanical index range [4]. Mechanical index (MI) is expressed as in Eq. (2.1):

$$\mathrm{MI} = \frac{\mathrm{PNP}}{\sqrt{fc}} \qquad (2.1)$$

where PNP is the peak negative pressure of the ultrasound pulse given in MPa and normalized by 1 MPa, and fc is the center frequency of the ultrasound signal, given in MHz and normalized by 1 MHz.

In drug delivery, ultrasound can be used for both guiding and triggering purposes. Therefore, both the diagnostic (imaging) and therapeutic (triggering, cavitation) ranges of the MI need to be considered for safe ultrasound mediated drug delivery. Table 2.2 presents the recommended ranges of MI for medical diagnostic applications.

Mechanical index (MI)	Recommended medical application
Less than 0.3	For medical diagnostic applications
Between 0.3 and 0.7	Cause minor damage to soft tissues such as human intestines
Greater than 0.7	Unsafe for diagnostic applications

Table 2.2 Recommended ranges of MI for different medical diagnostic applications [30] [31].

For the case of therapeutic applications, the FDA set the upper limit of MI to be 1.9 in order to reduce direct effects of ultrasound pulse on tissues [4] [26]. If one also considers cavitation, then the recommended upper bound value for MI is about 0.7 above which significant risks of cavitation can be observed [22] [27] [30] .

2.2 Antibubbles

An antibubble is a thin film of gas containing droplet/s of liquid, unlike a gas bubble, which is a sphere of gas surrounded by a liquid (see Figure 2.2). The life time of antibubbles is influenced by the electrical potential between the gas-liquid interfaces. In order to prevent the core droplet/s from touching the outer bubbles surface, this electrical potential should be equalized.

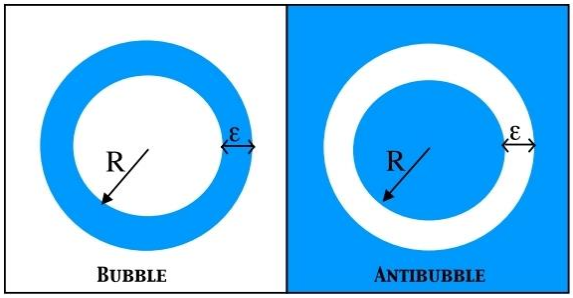

Figure 2.2 Structure of a bubble (left) and an antibubble (right) with an inner radius R and thickness of fluid/gas shell ε. The blue regions represent the liquid phase and the white represents gas [32].

An antibubble can also be defined as a regular bubble that contains a liquid droplet. The number of droplets that is found inside the antibubble can be single or multiple. Figure 2.3 presents an antibubble with multiple core droplets. Its existence was first reported by Hughes and Hughes in 1932 [32] when it was discovered that a thin film of air can enclose a liquid globule in a surrounding liquid. The liquids forming the globule and the surrounding liquid are the same. The term antibubble is then coined for this liquid–gas entity by Connett in 1974 [33].

Figure 2.3 Optical microscopy image of stable antibubble with multiple cores [14].

Regardless of their similar structure and composition, bubbles and antibubbles have very different properties. The main differences are their life time, light refraction manner and oscillation property. Under normal conditions, antibubbles are short lived and stay only few second or less while gas bubbles could live up to several minutes. Though, there have been efforts in the literature on ways to increase the life time of antibubbles. Nevertheless, life time of antibubbles depends on the electrical potential between the inner and outer liquid-gas interface. If this potential can be equalized, an antibubble with longer lifetime than air bubble, on the order of at least tens of hours, can be produced. In terms of their light refraction manner, since antibubbles contain liquid droplets, light passing through them will refract in the same way as a rainbow is formed and this will make them to be brighter than bubbles. The third difference is their oscillation property. This is mainly due to the compressibility of the air shell while both bubbles and antibubbles oscillate upon sonication [34]. The antibubble oscillation is asymmetric since its core droplet can be considered incompressible. Due to this reason, antibubbles can generate higher harmonics even if ultrasound with low acoustic amplitude is applied, which makes them suitable candidates for ultrasonic harmonic imaging and drug delivery. On the other hand, air bubbles generate limited harmonics when subjected to lower acoustic amplitudes.

2.2.1 Structure and Composition of Antibubbles

Structure and composition of antibubbles depends on the method in which they are produced. There are several methods of antibubble production [35]. The easiest way involves gently dropping/pouring of small amount of the same liquid as the sample over the gas liquid surface. As a result, a gas film is formed around the drop of liquid which separates it from the existing liquid. The stability of this formed antibubble depends on the Rayleigh – Plateau instability. Another method of antibubble formation could be from the breaking liquid flow under the effect of surface tension, which is used by most researchers. Some improvements were also made to this method such as preventing electrical potential difference at the gas-liquid interface due to triboelectric effects (attraction) by adding an electrical connection and also creating oscillation in the incident jet by vibrating the nozzle. Other totally different approaches were also used by some researchers. Among these, the most practiced methods include: capillary flow focusing to generate micron sized antibubbles, the coalescence between two bubbles to generate millimeter sized antibubbles, and the most known method is freeze-drying method which involves water-in-oil-in-water double emulsification process for a purpose of stabilizing the particle and then freeze-drying to remove both the water and the oil, and finally reconstitute the resulting powder in water.

The experimental dataset used in the current study contains antibubbles which are created by following the process of water-in-oil-in-water double emulsification. This emulsification process was done between maltodextrin solution and hexane oil, with the use of hydrophobised fumed silica particles as an emulsifier. The water has 25% carbohydrate maltodextrin content so that the volatility of the hexane oil is maintained. Even though the dataset contain two types of antibubbles composed of varying amounts of endoskeletal content, only one type of antibubble is used since there were far fewer data on the other. The first type of antibubble which is used in this research contained liquid cores of 2 vol% endoskeletal content and the second type of antibubble, though not used in the current study due to the very limited data size, contained liquid cores of 10 vol% endoskeletal content [36]. The difference in endoskeletal content of the two types of antibubbles was made of hydrophobically modified Zano 10 Plus zinc oxide nanoparticles (Umicore, Brussel), each having a diameter of around 30 nm. The addition of AerosilR R972 hydrophobised fumed silica particles made the antibubble stable (Evonik Industries AG, Essen, Germany). An ultrasound probe is used to disperse the silica particles

within the emulsion, which has average size of well below 1 µm. Once the double emulsion is done, it is frozen and freeze dried to remove both the water and hexane oil. Then the emulsion is reconstituted in an aqueous solution leading to formation of antibubble suspension [37].

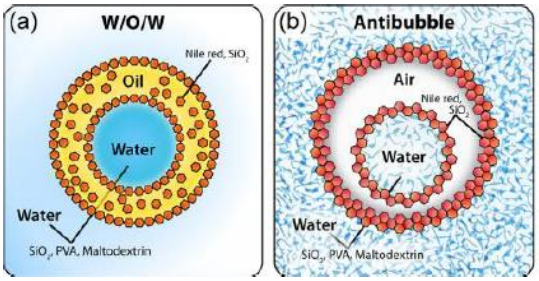

Figure 2.4 (a) water-in-oil-in-water double emulsion template (b) antibubble's structure after the emulsion is freeze-drying and reconstituted in aqueous solution [13].

To make up the experimental samples, 5 mL of 049-16797 distilled water was used to be combined with 5 mg of freeze-dried antibubbles (FUJIFILM Wako Pure Chemical Corporation, Chuo-Ku, Osaka, Japan). Then a 15 mg FALCONR high quality polypropylene conical tube was used to mix the sample by shaking it for one minute. Then finally, 200 µL of the sample was pipetted into the observation chamber [18].

2.2.2 Drug Loading in Antibubbles

Antibubble is a micron scale particle just like microbubble. They both undergo process of sonoporation when exposed to ultrasound wave. Encapsulating drug into such kind of micron scale particles is advantageous since it allows targeted drug release, increase permeability of the drug though the blood vessel directly to the target area, improve bioavailability of the drug, and minimizing its toxicity to the healthy tissue. The drug loading occurs during production phase of the drug carrier [38]. The amount/dose of the drug that can be delivered depends on the amount of antibubble injected and the amount of drug loaded in each antibubble [4]. The amount of the drug loaded per an antibubble can vary depending on the type and size of the antibubble, the type of the drug and the loading mechanism. Different loading strategies of antibubbles have been studied, that includes incorporating the drug inside the core droplet/s or the gas shell. It may rely on hydrophobic and hydrophilic behavior of the drug. According to different literature, stable antibubbles have drug loading volume approximately half of their entire volume which makes antibubbles to have higher loading capability than regular microbubbles [14].

2.2.3 Requirements of Antibubbles as a Drug Carrier

In drug delivery, antibubbles are the most recent advancements to be used as a drug carrier. In this approach, the main focus is to have a safe and accurate drug delivery. For the antibubbles to assume such characteristics, their design and formulation play an essential role. One of the major side effects in drug delivery is damaging of healthy cells and biological systems due to different factors such as wrong targeting, toxicity, dosage, undesired immune response and unwanted bio-effects as a result of higher inertial cavitation. In order to overcome these problems, the drug carrier should pass through different requirements such as ability to encapsulate enough amount of drugs, need to be small enough (<10 μm) to have the ability to reach the target site by passing through different biological barriers, fragmentation and drug release at the target matching the therapeutic requirement, stability, and non-toxicity [35].

2.2.4 Ultrasonic Response of Antibubbles

When an antibubble is subjected to an ultrasound pulse, it causes it to oscillate, dynamically depending on the ultrasound, generating spherical wave which radiates outwards [28]. When the antibubbles oscillate, they undergo different phenomenon including a series of expansion and contractions together with translocation as well as merging and splitting if there are nearby antibubbles that interact with them [29]. Fragmentations of the antibubbles occur above a certain threshold of the applied ultrasonic pressure. Intuitively speaking, fragmentation is a process of breaking down into fragments. These phenomena depend on the applied ultrasonic pressure and also the resulting maximum expansion of the antibubbles relative to its original size [18].

The oscillation of antibubbles can be of two types depending on the ultrasonic pressure applied [28] [29] (see also Figure 2.5 A). When they are subjected to low pressure ultrasound wave, they will oscillate repeatedly with series of stable contractions and expansions but will not undergo fragmentation. Such type of oscillation is known as stable oscillation. Increasing the ultrasonic pressure makes the antibubbles to experience inertial cavitation which leads them to expand to a much larger size followed by a maximum contraction (collapse) and finally fragmentation (see also Figure 2.5 B).

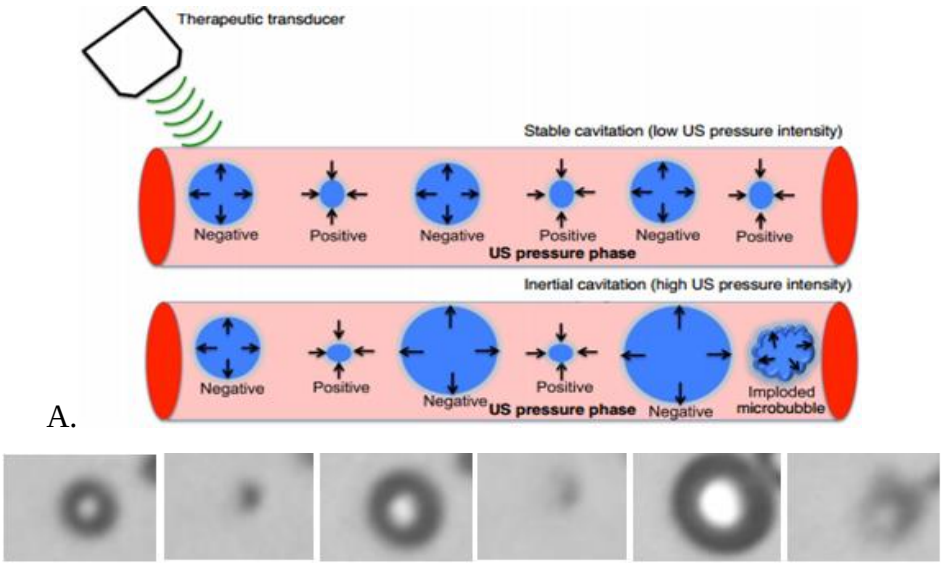

Figure 2.5 (A) Schematic drawing of stable and inertial cavitation phenomenon [4], (B) Experimental antibubble at different frames before, during and after applying ultrasound pulse with 0.6Mpa acoustic pressure.

2.2.4.1 Oscillation

Oscillation of bubbles under high acoustic pressure pulse is nonlinear and symmetric [18] [35]. In the case antibubbles, however, expected oscillation under sonication is still non-linear but more asymmetric. This is due to its incompressible droplet core/s. When we consider the effect of size of the droplet on its oscillation, theoretically larger droplet cores lead to higher excursion since they create larger pressure inside of the antibubble.

The oscillation of bubbles is governed by the Rayleigh-Plesset formulation, which is an ordinary differential equation (ODE) [14] [18]. The ODE is modified for antibubbles having core droplet and is given by the following second order, non-linear ODE:

$$R\ddot{R} + \frac{2}{3}\dot{R}^2 = \frac{1}{\rho}\left[\left(\rho_0 - \rho_v + \frac{2\sigma}{R_0}\right)\left(\frac{R_0^3 - R_d^3}{R^3 - R_d^3}\right)^{\gamma} + \rho_v - \frac{2\sigma}{R} - \frac{4\eta\dot{R}}{R} - \rho_0 - P(t)\right] \quad (2.2)$$

where R_0 = equilibrium radius, R = instantaneous radii, $\acute{R}$ = the instantaneous velocity, ρ = liquid density, P(t) = the ultrasound pressure, ρ_0 = ambient pressure, γ = polytropic exponent of the gas, ρ_v = vapor pressure, μ = viscosity of the surrounding fluid, σ = the surface tension, $\ddot{R}$ = the corresponding acceleration of expansion or contraction, Rd= radius of the internal liquid droplet core of the antibubble.

According to previous studies, Equation (2.2) results in more asymmetric radial excursion with increase in ultrasound pressure [18]. Meaning as the inertial cavitation due to high pressure ultrasound pulse increases, the inertia of the antibubble become larger than the applied ultrasound pressure, which results in highly asymmetric oscillation where positive excursion becomes much larger than negative excursion. Under ultrasound pulse with lower amplitude, the oscillation is stable. The antibubbles expansion depends on their initial size and core size in addition to ultrasonic pressure [19] [18]. They expand more relative to their equilibrium size.

2.2.4.2 Fragmentation

It has already been studied that when microbubbles and antibubbles are put under pressure using periodic ultrasound pulses, they experience fragmentation, while their destruction patterns are highly dependent on the magnitude of the applied pulses. In case of microbubbles, once in sonication mode, for fragmentation to happen, sufficiently big expansion followed by collapse is required. Same applies to antibubbles but since the core droplet of antibubbles is incompressible, its contraction is limited compared to bubbles [18]. Having sufficiently big expansion, concentrates enough energy to break apart the antibubble. During collapse, the kinetic energy will be greater than the surface energy. In this regard, given an antibubble with certain initial size, developing a tool that allows determining the destruction threshold could be of vital importance in studying the interaction of antibubbles with ultrasound pulses.

Based on different literatures reviewed, there are mainly two mechanisms that are possible causes for fragmentation [39]. The first one is Rayleigh–Taylor instability and the second one is parametric instability though the two are not necessarily mutually exclusive. The Rayleigh–Taylor instability is caused by positive wall acceleration and very large negative wall velocity. Parametric instability, on the other hand, is caused by shape instability which is the result of radial oscillations (expansion and contractions). The source of this instability is higher order spherical harmonic oscillation which can be due to sonication with higher acoustic pressure waves. The quantification of destruction threshold of antibubbles in the current research work was entirely based on the second mechanism. There is also a theory such as the Blake's threshold approximation gives us a theoretical relationship between the initial size of bubbles and their destruction threshold based on an idealistic model of antibubbles [40]. According to Blake's, the critical radius of an antibubble that results in fragmentation is about twice its initial radius (Equation 2.3).

$$Rcr \approx 2Ro; \quad (2.3)$$

Where R_{cr} is the critical radius and R_0 is initial radius of the antibubble.

Here the critical radius, also called Blake's critical radius, is where all bubbles with radius less than R_{cr} will stay in stable condition and when the radius exceeds R_{cr}, it will experience fragmentation. In other word R_{cr} is the maximum radius which leads to instability of the bubble.

Another study reported findings that showed that Blake's approximation is not a good approximation for destruction threshold [8].

2.2.4.3 Coalescence

Coalescence is a phenomenon during sonication where antibubbles at close proximity collides one another due to experiencing secondary radiation force during expansion [18] . For the given two colliding antibubbles with radius R_1 and R_2, the resulting harmonic mean radius (R_m) after antibubbles coalesced can be calculated as (Equation 2.4):

$$\frac{2}{Rm} = \left(\frac{1}{R1}\right) + \left(\frac{1}{R2}\right) \quad (2.4)$$

In this chapter it was discussed about ultrasound and its applications in drug delivery together with antibubbles and their theoretical background. Antibubbles are still under investigation to be used as drug carriers. The process of drug delivery basically relies on the interaction between the drug carrier (antibubble) and an acoustic wave. Their interaction is also known as acoustic cavitation, which creates a path for the penetration of the drug to the target region. However, if this cavitation is greater than the threshold, it will cause undesired bio-effects. According to FDA, the threshold for MI of an applied ultrasound pulse is set to be 0.7, where significant risk of cavitation can occur if the MI is greater than this threshold. In addition, the theoretical concept behind antibubbles needs a proof of concept with the help of experimental analysis. The next chapter discusses how experimental analysis is done to prove some of the existing theoretical concepts using image processing of gray scale images of antibubbles taken over a high speed photographic camera.

Chapter 3: Antibubble Size Distribution Analysis for Destruction Threshold Determination

Gray-scale videos (image frames) of antibubbles acquired experimentally were analyzed in the current study and a digital image processing scheme was developed to perform effective size distribution analysis as well as destruction threshold determination. The dataset contain pictures of antibubbles exposed to ultrasound wave with varying acoustic amplitudes. Each video was composed of 256 frames and a frame based digital image processing algorithm was developed. This chapter provides details on the experimental setup used to obtain the data and the digital image processing algorithm. The image processing algorithm involved basic stages including pre-processing and feature based segmentation steps.

3.1 Experimental Setup and Procedure

The experimental setup used to generate the gray-scale videos of the antibubbles is depicted in Figure 3.1. The setup allows a clear observation and recording of the effects of ultrasound on antibubbles. The experiment involves the generation of a sound field, which is capable of targeting a 200µL sample of water-immersed antibubble solution [18].

The ultrasound pulse is generated using an arbitrary AFG320 signal generator (Sony-Tektronicx, Shinagawa, Tokyo, Japan) and the signal generator is used together with UOD-WB-1000 wide-band power amplifier (TOKIN Coporation, Shiroishi, Miyagi, Japan). The signal generator is connected to a transducer having an aperture of 50mm and a radius of 70mm. This transducer produces three cycles of ultrasound pulse having central frequency of 1MHz for each experiment. Central frequency of 1MHz is selected for the ultrasound pulse taking the attenuation of tissue into consideration and since the pulse travels poorly in air, a water immersion medium is used for the transducer [18]. Experiments were carried out under ultrasound pulse of four different acoustic amplitudes (1V, 2V, 3V and 5V) which correspond to acoustic pressure values (PNP) of 0.2 MPa, 0.4 MPa, 0.6 MPa, and 1 Mpa, respectively.

The videos are recorded by using high-speed camera attached to an inverted microscope. IX70 inverted microscope with LUMPlan FI/IR 40x (NA 0.8) objective lens was fitted to the microscope to have full view of the observation chamber. The observation chamber is created by

drilling a 10mm hole through the bottom of the water tank. The observation chamber is illuminated with a halogen lamp. The type of high-speed camera used is HPV-X2 with shutter speed set considering v10 million frames per second, with a total horizontal field of view of 145µm [18]. Each experiment lasts about 25.6µseconds, while each ultrasound pulse lasts 3µs.

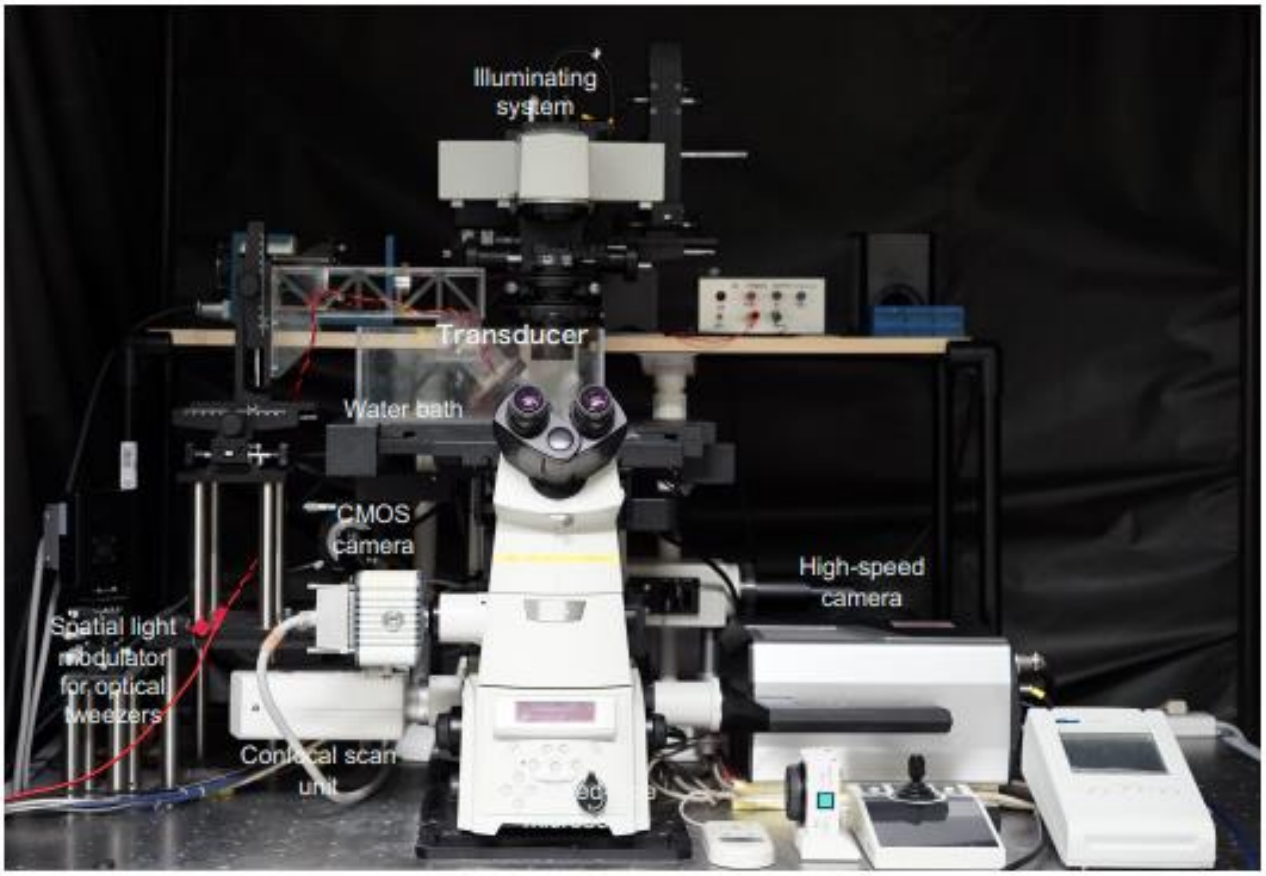

Figure 3.1 Experimental setup [18].

The experimental data includes two different samples; both of them contain antibubbles with different endoskeletal contents. In each case, images were taken before, during and after sonication with varying amount of acoustic amplitude. Only one of the samples has been used in the current study due to limited sample size on the second. Total of 55 gray scale videos each containing 256 frames were used to observe the size distribution and determine destruction threshold for manually selected antibubbles.

3.2 Algorithm

Figure 3.2 below presents the general schematic of the proposed method which includes pre-processing, feature extraction, segmentation and finally post processing for size distribution and determination of the destruction threshold. Each of these steps is explained in the subsequent sub-sections.

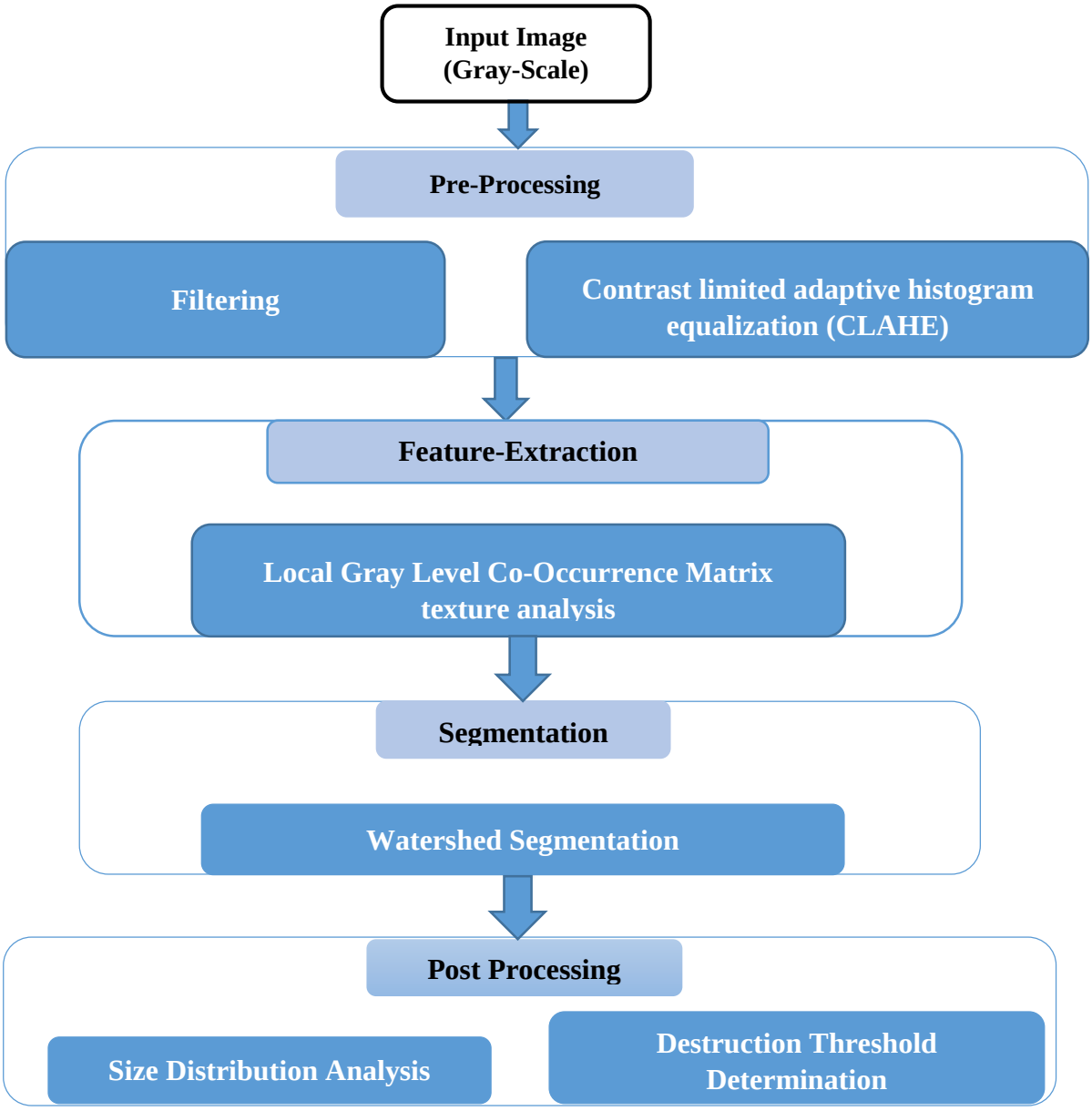

Figure 3.2 General block diagram of the proposed method.

3.2.1 Image Pre-processing

The image pre-processing step consists of frame separation and image enhancement [41]. The image enhancement techniques utilized were filters for noise reduction and histogram equalization.

- ***Filtering:*** It is very subjective area and can be done in two domains, spatial and frequency domain [42]. The spatial domain filtering techniques are applied directly on the images actual pixels. Some of the spatial domain fires include mean filter, averaging filter and median filter. The filters are applied based on the type of noise involved. For the high speed camera pictures of the antibubbles, salt-and-pepper (impulse) type of noise were visible on each frame and a one pass median filter was applied prior to histogram equalization. Figure 3.3 presents a typical gray-scale image of antibubbles considered in the current study before and after the application a one pass median filter with different window sizes. Application of the median filter on the different frames included in the database showed that the 3x3 window size is preferred to deal with the pepper noise that is present in the images as the higher window sizes tend also to lose important image details in the process.

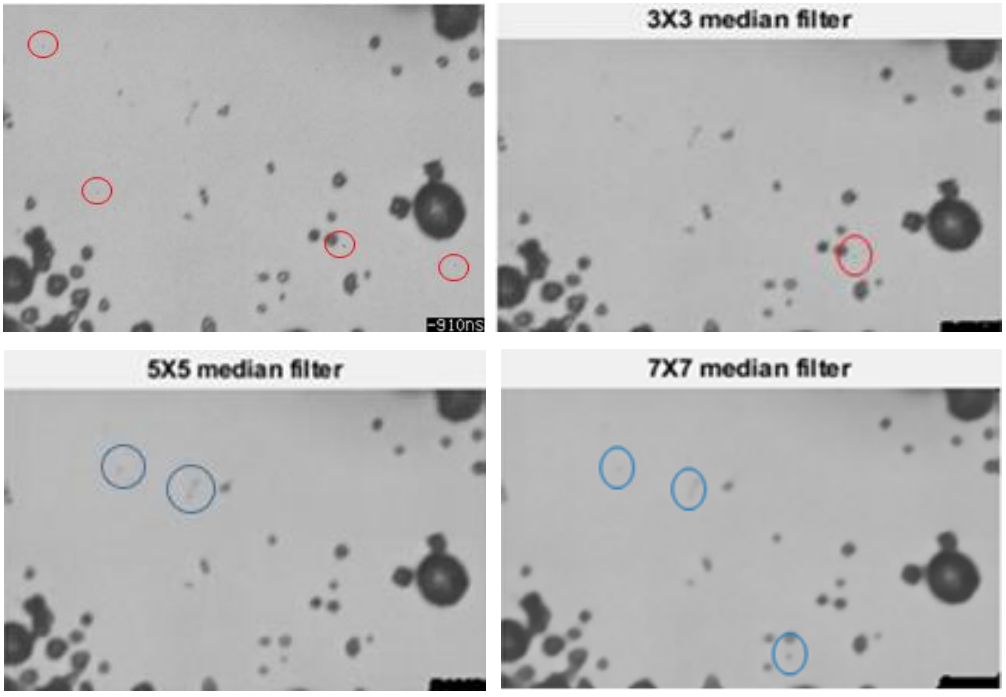

Figure 3.3 Original image of the antibubbles (top left) and image after median filtering with window size 3x3 (top right), 5x5 (bottom left) and 7x7 (bottom right).

- The red circles on the original images shown in Figure 3.3 indicate areas containing pepper noise. The application of the 3x3, 5x5 and 7x7 median filters clearly shows the effective removal of the pepper noise. In the current work, one pass of the 3x3 median filter has been used for further processing as the higher window size median filters tend to remove useful image information, i.e. smaller antibubbles. The blue circles shown in Figure 3.3 show antibubbles washed away by the higher window size median filter.
- ***Contrast Limited Adaptive Histogram Equalization (CLAHE)****:* Following the median filter operation, a histogram manipulation technique was applied on the digital negative (image negative) version of the image targeting further enhancement. That was done using the contrast limited adaptive histogram equalization (CLAHE). CALHE, as opposed to global histogram equalization, enhances images considering local image characteristics. In addition based on the literatures, it is a novel approach to enhance video (image sequence) [43] [44].
- The CLAHE operation was followed by imclearboarder operation which simply eliminates those objects found at the border, which provide only partial information about antibubbles that are found at the boarders. Figure 3.4 presents the application of CLAHE on median filtred images of antibibbles followed by the imclearboarder operation before, during and after sonication.

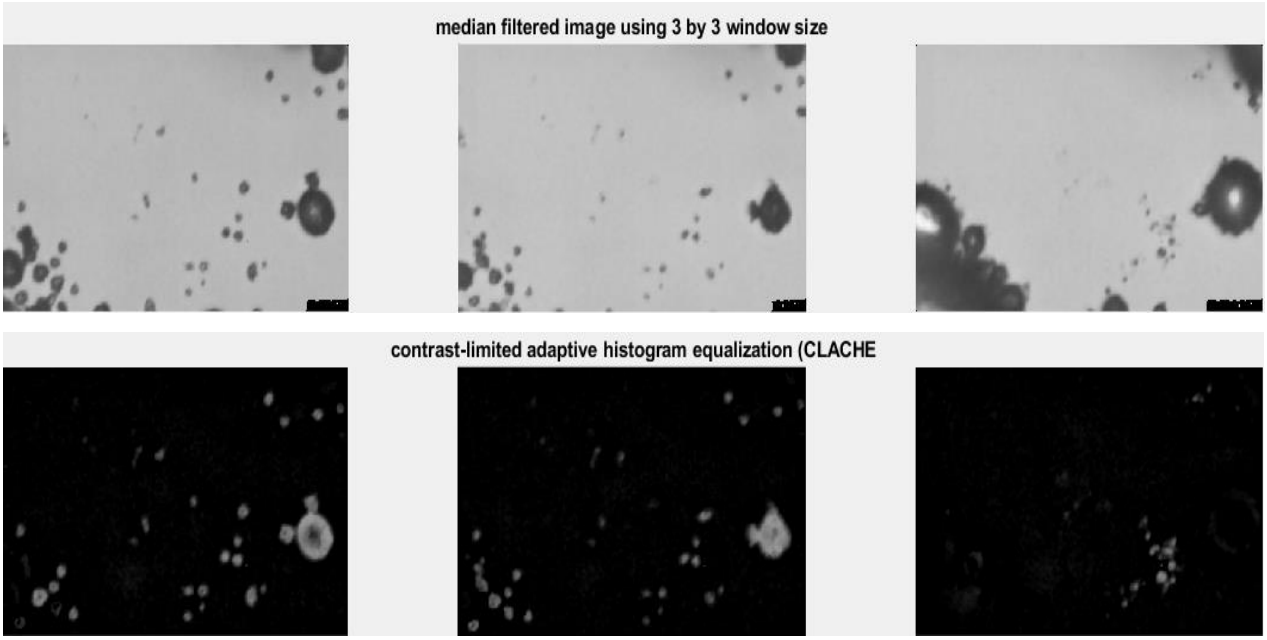

Figure 3.4 Original image of antibubbles before, during and after sonication (top: left to right), and images after applying contrast limited adaptive histogram equalization (bottom).

3.2.2 Feature Extraction

Feature extraction is an image processing technique which is used to obtain visual information of the image for further processing such as image classification and segmentation of an object [45]. Features can be extracted which are either domain specific or general such as texture, color and shape. Texture is a spatial arrangement of pixel intensities which tells the visual characteristics of the object surface. It is highly applicable in different image processing areas including medical image analysis. One widely used method of extracting texture features from gray scale images makes use the gray level co-occurrence matrix (GLCM), which is a second order statistical method used to derive useful texture descriptors, and could be implemented either locally or globally.

GLCM is a square matrix that shows the probability of occurrence of two different neighboring pixel values at a given offset (with respect to given distance and orientation) [46]. The elements in the GLCM indicate the number of occurrence of a reference pixel with its neighboring pixels. The GLCM allows certain properties be exposed about the spatial distribution of the gray levels in the image and the spatial relationships between pairs of pixels are calculated at various orientations. In the current work, in order to create the GLCM from a given image, Matlab built-in function *graycomatrix* () was used. By default, the spatial relationship is searched horizontally (0^o) and only with the very next neighbors where the displacement value is just one unit (see Figure 3.5). But it can be set at different orientations and displacement (off-sets).

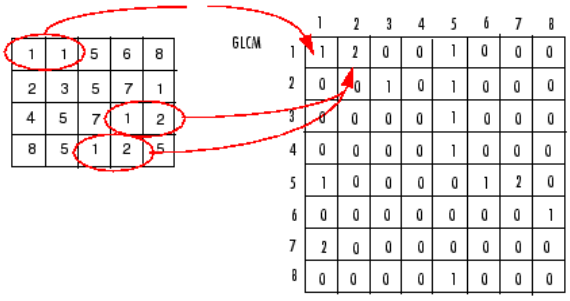

Figure 3.5 Gray level co-occurrence matrix computed at 0 degrees.

The elements (i, j) in the GLCM are simply the frequency of pixels with value i occurring at specified orientation to a pixel value j in the input image [46]. In the current work, all eight neighborhood directions, i.e. 0, 45, 90, 135, 180, 225, 270 and 315 degrees, were considered for the GLCM calculation. So the offset is described as:

Offsets = [0 1;-1 1;-1 0;-1 -1; 1 1; 1 0; 1 -1; 0 -1];

The GLCM is computed locally (with eight offsets) over a translating localizing window of size 3x3 and the matrix that results by summing the GLCM values along the eight directions was used to compute the texture features. These are essentially "Haralick" features computed locally [46]. The chosen feature value will then replace the central pixel. This step is repeated until all pixel positions are traced before the final texture map is generated. Several features from the GLCM matrix can be computed, the so called texture descriptors, and the resulting texture map is used as input to the proposed texture based segmentation scheme. Nine "Haralick" texture features were computed: Contrast, Correlation, Energy, Homogeneity, Maximum Probability, Cluster Shade, Cluster Prominence, Entropy and Dissimilarity. Figure 3.6 presents the local texture maps generated using four selected features: contrast, cluster prominence, max probability and cluster shade. Once the texture maps are generated, a qualitative test was carried out in terms of their performance in enhancing the antibubble images making them ready for final segmentation (see Appendix II).

Given the probability co-occurrence matrix, $\mathrm{P}(i,j)$, for a given offset distance d and direction θ, the texture features were mathematically computed as follows [47]:

$$\text{Contrast} = \sum_{i=0}^{L-1} n^2 \sum_{i=0}^{L} \sum_{j=0}^{L} \mathrm{P}(i,j), \quad \text{where, i – j = n} \tag{3.1}$$

$$\text{Cluster shade} = \sum_{i=0}^{L-1} \sum_{j=0}^{L-1} \left(\mathrm{i} + \mathrm{j} - \mu_x - \mu_y\right)^3 \mathrm{P}(i,j) \tag{3.2}$$

$$\text{Cluster prominence} = \sum_{i=0}^{L-1} \sum_{j=0}^{L-1} \left(\mathrm{i} + \mathrm{j} - \mu_x - \mu_y\right)^4 \mathrm{P}(i,j/d) \tag{3.3}$$

$$\text{Maximum Probability} = \max_{ij}\{\mathrm{P}(i,j)\} \tag{3.4}$$

where μ is the total mean and μ_x and μ_y are mean of the row and column sums of $\mathrm{P}(i,j)$ given by

$$\mu_x = \sum_{i=0}^{L-1} i \sum_{j=0}^{L-1} \mathrm{P}(i,j/d) \tag{3.5}$$

$$\mu_y = \sum_{i=0}^{L-1} j \sum_{j=0}^{L-1} \mathrm{P}(i,j/d) \tag{3.6}$$

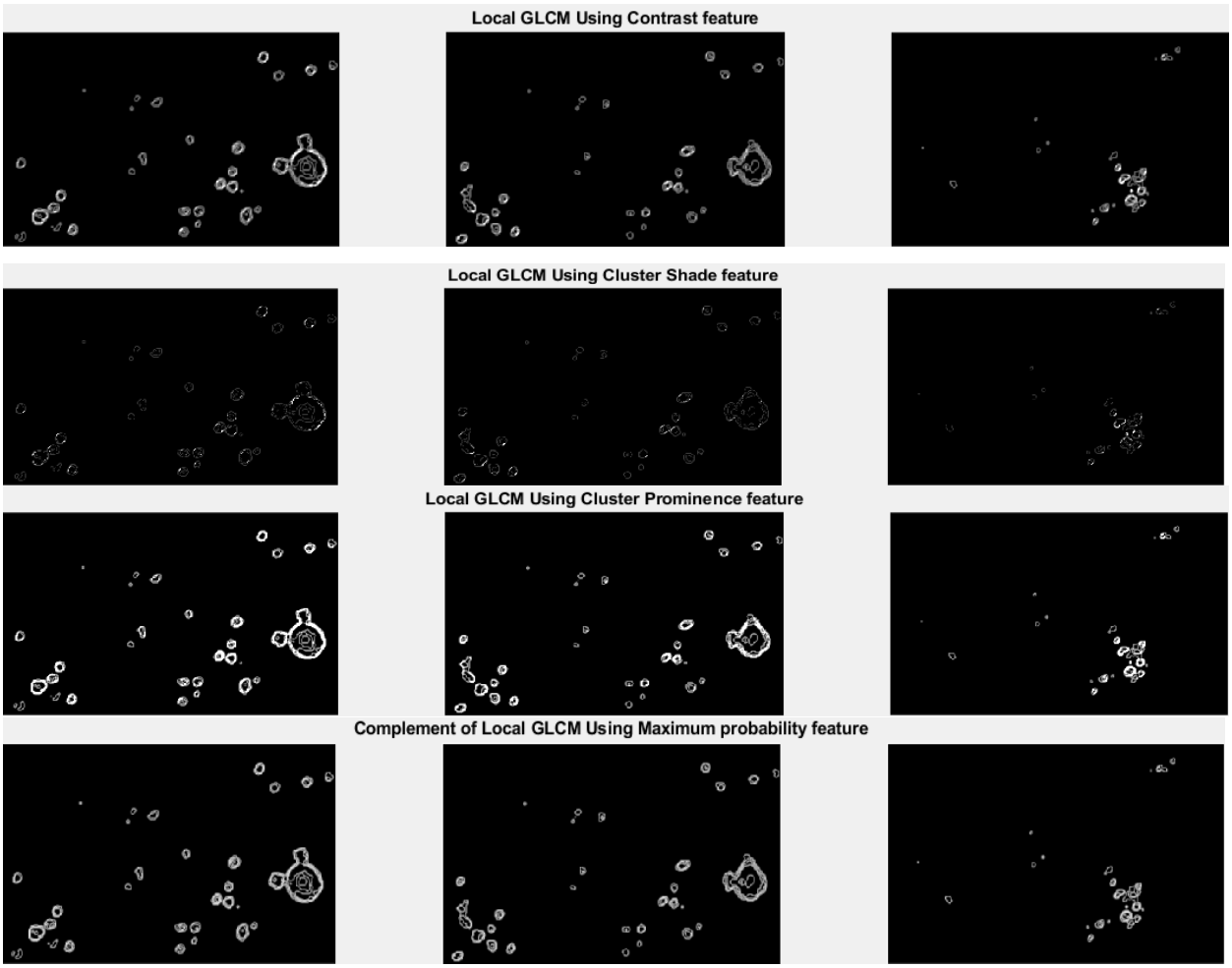

Figure 3.6 Texture features using local GLCM computed on the pre-processed antibubble images shown in Figure 3.4.

Among the nine computed texture features, maximum probability offered the best results in terms of enhancing the antibubbles from their background. The selection of texture features is made majorly based on a qualitative evaluation in terms of their ability to amplify antibubbles against their background, their efficacy in differentiating very nearby antibubbles as well as their performance in identifying very small antibubbles. Cluster prominence also performed very well but had limitations in differentiating very nearby antibubbles (see for example the red circles in Figure 3.8 (a)).

3.2.3 Image Segmentation

Image segmentation is a technique used to divide images into parts (also called segments). Even though there is no clear standard for classification of segmentation techniques, the type of segmentation technique to be used can be varied depending on different factors, such as: the

approach (“bottom-up”, “top-down”, and “graph based”); the application area: the image type (gray scale, colored or binary); the type of feature (intensity, texture, motion, color); and mathematical foundation (morphology, image statistics, and graph theory) [41]. Among those techniques, threshold method, edge based method, region based method, clustering method, watershed based method, PDE (partial differential equation) based method and ANN (artificial neural network) are the basic and most commonly used techniques [48]. These all techniques follow three basic segmentation approaches: region-based, edge based and hybrid approaches. Another general classification categorizes segmentation techniques into three: structural, stochastic, and hybrid techniques. Structural segmentation techniques are based on structural information of the region to be segmented. Whereas the stochastic techniques are based on discrete pixel values of the image and hybrid techniques use the concept of both structural and stochastic segmentation techniques. Some of the basic and most commonly used segmentation techniques are described below.

- ***Thresholding****:* is the simplest method of segmentation that is based on intensity [41]. This technique is useful to segment the object of interest (foreground) from the background. There are various thresholding techniques including simple global thresholding, Otsu thresholding, and adaptive thresholding. The major drawbacks of the thresholding based segmentation are that they are entirely based on intensity magnitude information, are sensitive to noise (especially salt and pepper noise) and also they are not efficient in segmenting overlapping objects [49] [50].
- ***Edge Based:*** edges are image points where an abrupt change in gray level is observed and usually occurs at object boundaries [51]. Edge based segmentation techniques first detect the edge points and then establish the boundary by connecting the edge points to segment the area of interest. Gradient based and laplacian based methods are two commonly used edge based segmentation methods. These techniques include: Robert cross gradient method, Prewitt method, Sobel method, Laplacian of the Gaussian method, and Canny method. The major limitation of these methods is that they segment objects based on discontinuity detection which as a result create disconnected edges and they are generally sensitive to noise [50] [49].
- ***Region Based:*** segments the object of interest based on similarity information in a given image. It incorporates the connectivity of pixels to decide if the pixel belongs to same object

(region) or not. The basic region based segmentation techniques are region growing and region splitting & merging [49]. The region growing approach is based on the idea of growing a seed (initial pixel) or group of seeds which is controlled by connectivity of the pixels to segment object of interest. The seed is obtained either manually or automatically for a specific application. The region splitting & merging method starts with region splitting which will divide the given image into smaller regions until each sub-image can be considered to be homogeneous based on some criteria. Then based on the homogeneity criteria, it performs region merging [42]. The major difficulties in this approach include appropriate seed point selection and the stopping mechanism. In addition, it is sensitive to intensity variations and noise which often result in over segmentation [50].

- ***Clustering Based:*** segments an image into clusters based on pixels having similar character in an unsupervised fashion [48]. K-means clustering algorithm is one of the commonly used clustering approaches. One major difficulty in clustering based approaches is in trying to specify the number of clusters. Specifically, for K-means, specifying the K-value is a major difficulty especially having limited data set [50].
- ***Partial Differential Equation (PDE) Based:*** this method is based on differential equations and employed in a variety of applications, including image noise reduction and edge detection [48]. This method has the advantage of being the fastest, although it frequently results in blurred edges and boundaries affecting its performance when applied in segmentation.
- ***Artificial Neural Network (ANN) Based:*** involves a series of computational systems and is based on simulation of a learning process for decision making [52]. It has two main parts which are processing and learning. The processing element is done based on connected units (nodes), often called artificial neurons, and the learning is carried out by adaptation between the nodes. There exist different ANN architectures one can borrow without the need to write complicated program starting from the scratch. The major drawback of the ANN based approach is that it normally requires longer training time and sufficient data to train the system [50].
- ***Watershed Based:*** the watershed segmentation technique was proposed in 1990 by S. Beucler and F. Mayor [48]. Intuitively speaking, watershed is a ridge that divides an area having different drainage system. When it comes to segmentation, the term catchment basin

is used to represent the drainage that flows into different river systems and the ridgelines (watershed lines) represent the boundary lines in between (see also Figure 3.7) [52].

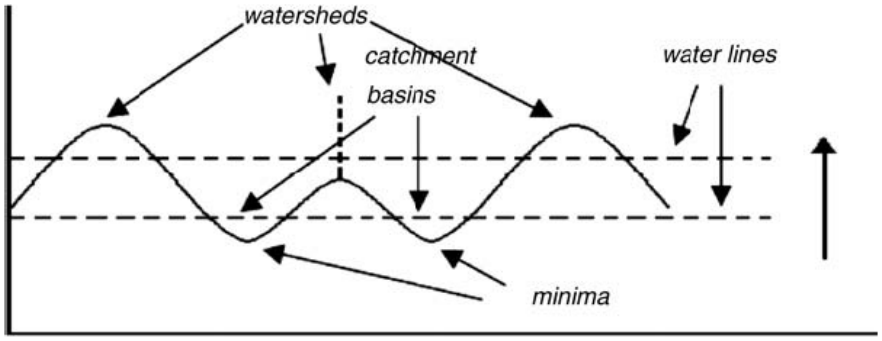

Figure 3.7 Watersheds and catchment basins [52].

- In watershed segmentation, a 2D gray scale image is treated as a surface (‘landscape’) with x, y coordinates and a height z which represents the gray scale intensity [42]. The basic concept here is that naturally water falling from above onto the surface is drained downwards to the nearest minimum point because of gravity. Those minimum points which are found at same point will be connected together to form a catchment basin. The lines that divide adjacent catchments are the watershed ridges. Similar explanation could be made for gradually flooded surface from below.

Selecting the appropriate and suitable segmentation technique is essential for further processing and effective analysis. Among the above mentioned segmentation techniques watershed segmentation was chosen in the current thesis work. Compared to the others, this segmentation technique is preferable for the purpose of segmenting very nearby or touching objects, which is particularly relevant in the current study as we are dealing with images of micron sized antibubbles where two or more of them could come closer when they are under sonication. Another interesting advantage of the watershed method is that it generally yields closed contours in indicating the exact position of object boundaries [50]. This is important since accurate size determination of the antibubbles requires their effective segmentation with a clear boundary. In addition it is fast, simple and intuitive segmentation technique [48].

Some literatures discuss possible limitations of the watershed approach one being the issue of over segmentation. As a matter of fact, the proposed segmentation approach is not just a watershed but it is a hybrid between texture analysis and watershed with a potential to avoid risk

of over segmentation. Such approach of marking the foreground objects (which are the antibubbles in our case and were marked through texture analysis) proceeding the watershed step has also been suggested in previous literatures [53] [54]. Figure 3.8 presents watershed segmented images of antibubbles and compares the performance of the max probability feature against cluster prominence. The figure clearly indicates that the max probability feature showed superior performance particularly in differentiating nearby antibubbles (see the red contours for example). Note that the entire segmentation algorithm was implemented in a Matlab environment.

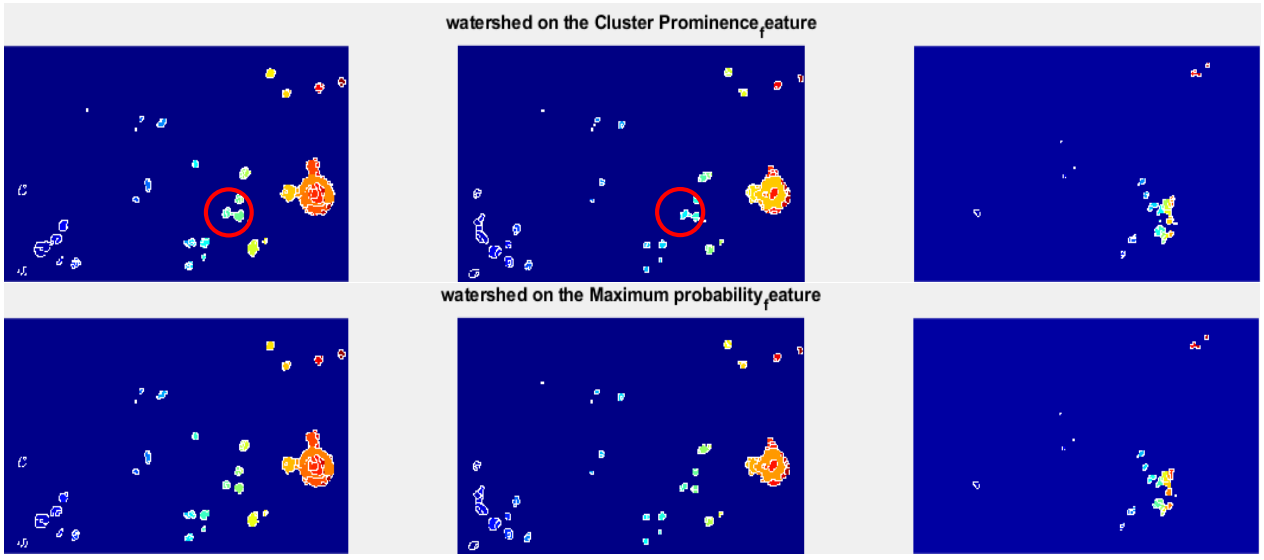

Figure 3.8 Watershed segmentation before (left), during (middle) and after (right) sonication: using cluster prominence feature (top) and using maximum probability feature (bottom).

3.2.4 Post Processing and Analysis

3.2.4.1 Size Distribution

Determination of the actual size distribution of the antibubbles followed the segmentation step and that was implemented using ImageJ software. In order to quantify the actual size of the segmented antibubbles, the pixel resolution of the images is required. The horizontal field of view of the microscope used in the experiment to generate the images of the antibubbles used in the current study was configured in such a way that 145 µm represents 400 pixels. Hence, for typical frame size of the antibubble images, which was 400 x 250, a pixel will be of dimension 0.3625µm. The number of pixels in a given segmented antibubble will be multiplied by this factor to compute its exact size in terms of its total area. Then size distribution of individual

antibubble is analyzed in terms of area-time curve. This is used to show the oscillation characteristics of antibubbles (with varying initial size) under different ultrasonic pressure and to determine their destruction threshold.

Figure 3.9 presents a sample ultrasound pulse that is used in the experiment for the current research and Figure 3.10 represents the corresponding theoretically expected response of standard antibubble presented here in terms of radius-time curve [18]. The ultrasound pulse assumed a peak-to-peak negative pressure of 0.2Mpa and consists of three cycles each lasting 1µs. The experiment takes a total of 25.6µs. The central frequency was 1MHz, chosen considering possible tissue attenuation.

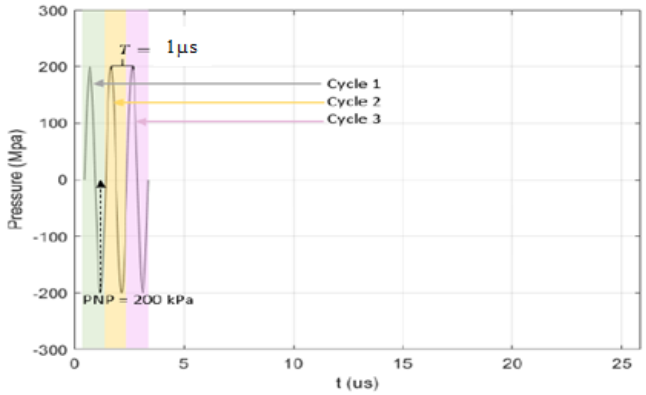

Figure 3.9 Representation of an ultrasound pulse with peak-to-peak negative pressure of 0.2 MPa (1V Amplitude) [18].

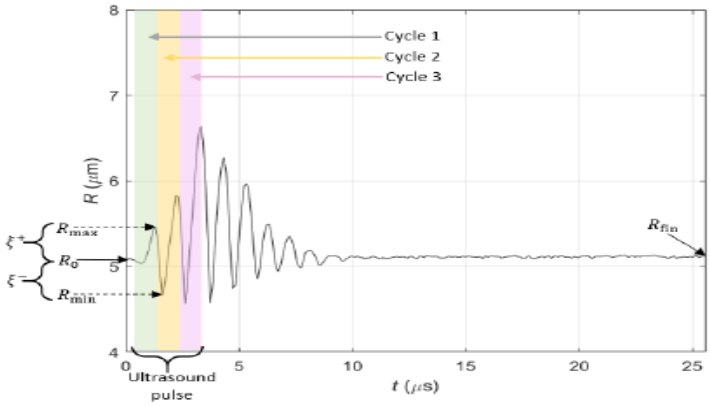

Figure 3.10 Radius-time curve of a standard antibubble under ultrasonic pressure of 0.2 MPa having three cycles; Ro is the initial radius, and R_{max} and R_{min} are the maximum and minimum radii after the first cycle, respectively. The time is in µs where the whole experiment took 25.6µs [18].

Similarly, size distribution of antibubbles under different ultrasound pulse pressure, i.e. 0.4 MPa, 0.6 MPa, and 1 MPa, were analyzed. Having the concept of radius-time curve of antibubbles in response to ultrasound pulse, the current research considered the size in terms of total Area. The size distribution of the antibubbles using their total area is expected to resemble the theoretically generated radius-time curve shown in Figure 3.10.

3.2.4.2 Destruction Threshold Determination

The last stage which follows quantification of the size distribution of the antibubbles is determining their respective destruction thresholds. That corresponds to the time when the applied ultrasonic pressure results in antibubble fragmentation. Based on the theory explained in section 2.2.4.2 in the previous chapter supported by the reviewed literatures, having sufficiently big expansion concentrates enough energy to destruct a given antibubble. Therefore, the current research determines destruction threshold in terms of maximum expansion (area) of the antibubbles which leads to their fragmentation with respect to its original size for a given ultrasonic pressure.

Chapter 4: Results and Discussion

This chapter provides results and discussion related to size distribution and destruction threshold determination. The size distribution is shown intermes of area-time curve. In order to determine the destruction threshold of a given antibubble with initial size (Ai), the predictability of maximum expansion is investigated and analyzed. Discussion is done on the experimental results by comparing it with existing theories.

4.1 Size Quantification

Before analyzing the size distribution of the antibubbles under sonication, the effectiveness of the proposed segmentation approach was first evaluated in terms of actual size quantification of antibubbles with known size. Figure 4.1 (a) presents a microscopic image containing antibubble with core droplet and (b) same antibubble losing its core. The antibubble is produced using the method of water-in-oil-in water emulsification followed by freeze drying using the procedure explained in the previous chapter. The approximate size of this antibubble (core + shell) was 61µm in diameter which is then shrinks to diameter of 55µm as a result of losing its droplet; these diameters were computed directly using ImageJ [37]. The proposed algorithm is used to segment the antibubble and its diameter is measured using ImageJ software using the procedure explained in the methodology section presented in Chapter 3.

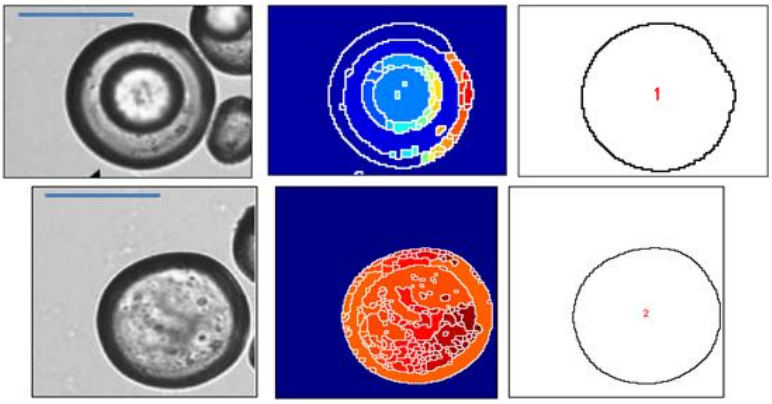

Figure 4.1 (top) Bright-field microscope image of an antibubble with core droplet; (bottom) bubble losing its core droplet: original gray scale image, segmented image and labeled image (left to right). Scale bar is equal to 50 µm

No	Specified diameter	Measured area	Measured diameter	Relative difference
1	61 µm	3237.831 μm^2	64.207 µm	5.2%
2	55 µm	2633.598 μm^2	57.907 µm	5.2%
		Average relative difference =		5.2%

Table 4.1 Size quantification of antibubbles with known size

The average relative difference between the measured and specified diameter is about 5.2%, showing the accuracy level of the proposed segmentation scmehe.

4.2 Size Distribution of Antibubbles

Experimental videos of the antibubbles under different ultrasound pulse were segmented using the proposed algorithm and the respective sizes were analyzed using imageJ. The actual horizontal (and vertical) dimension of individual pixels in the antibubble images was 0.3625 µm. Once the images are segmented, individual antibubbles were traced throughout the video frames they are found using imageJ. The area of the segmented antibubbles found in the different frames was then plotted against time and the area-time curves are generated.

The size distribution in terms of area-time curve was analyzed in order to study the antibubble interaction with ultrasound and determine the destruction threshold in terms of its maximum expansion with respect to its original size. As could be seen in the results presented, the distraction threshold is actually relevant when considering only high acoustic pressure ultrasound waves.

The size distribution pattern of the antibubbles was analyzed for the entire 256 image frames in case of lower acoustic pressure (i.e. 0.2 MPa and 0.4 MPa). As could be seen on the results, under lower acoustic pressure, the antibubbles show quite stable oscillation with no incidence of splitting, merging and fragmentation. However, in cases of higher acoustic amplitudes (0.6 MPa and 1 MPa), the antibubbles rather undergo a very dynamic oscillation and inertial cavitation. In this case it becomes very difficult and sometimes even impossible to follow a single antibubble after the first cycle of ultrasound pulse. Therefore, for antibubbles under 0.6 MPa and 1 MPa, the area-time curve was plotted only for the first 40 frames which correspond to 4µs. The first 40 frames were selected since it is enough to show the oscillation (response) of the antibubbles during the 3cycles of sonication.

Size Distribution under 0.2 MPa Ultrasonic Pressure

The first analysis was made on the response of antibubbles under ultrasound pulse having 1V amplitude (PNP of 0.2 MPa). Figure 4.2 presents a sample microscopic image containing antibubbles segmented using the proposed algorithm. Six antibubbles were manually identified on the segmented image for further size quantification and follow-up throughout the three cycles of ultrasound pulse, which was executed per image frame. Each antibubble is analyzed separately in terms of its total area computed using imageJ.

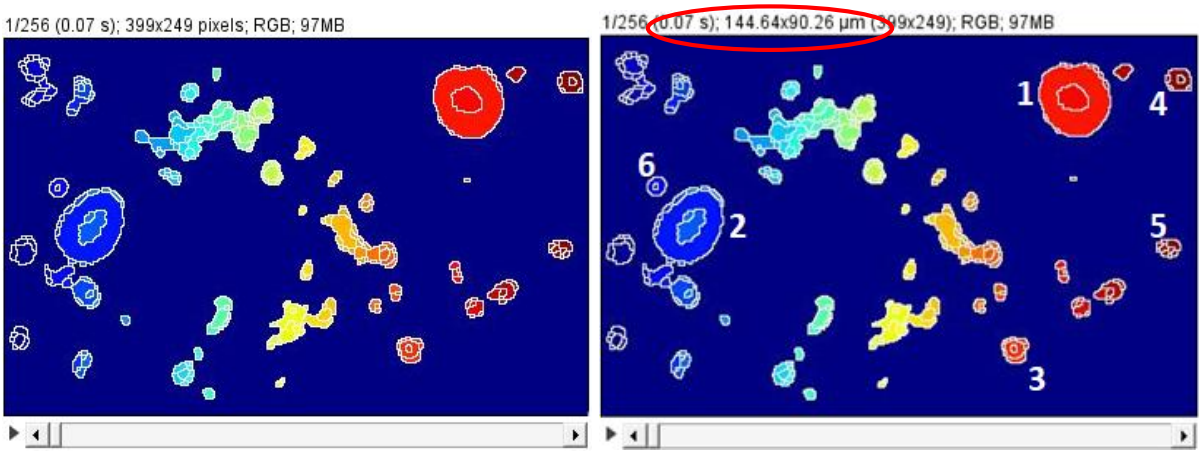

Figure 4.2 Segmented video footage of antibubbles under sonication of 0.2 MPa (left) and five antibubbles manually selected for further size distribution analysis (right).

Using imageJ, labeling individual antibubble makes it easier to follow its size distribution in all frames and a plot is acquired for area versus label of each antibubble. Figure 4.3 presents how individual antibubbles are labeled throughout the frame in order to get its corresponding size distribution.

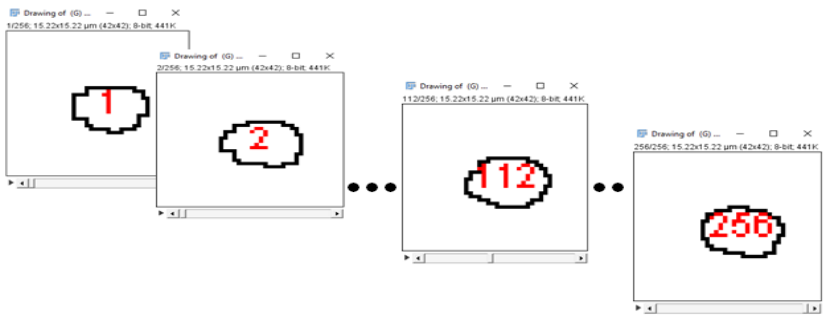

Figure 4.3 Labeled antibubbles at the 1st, 2nd, 112th, and at the last frame (which is 256th).

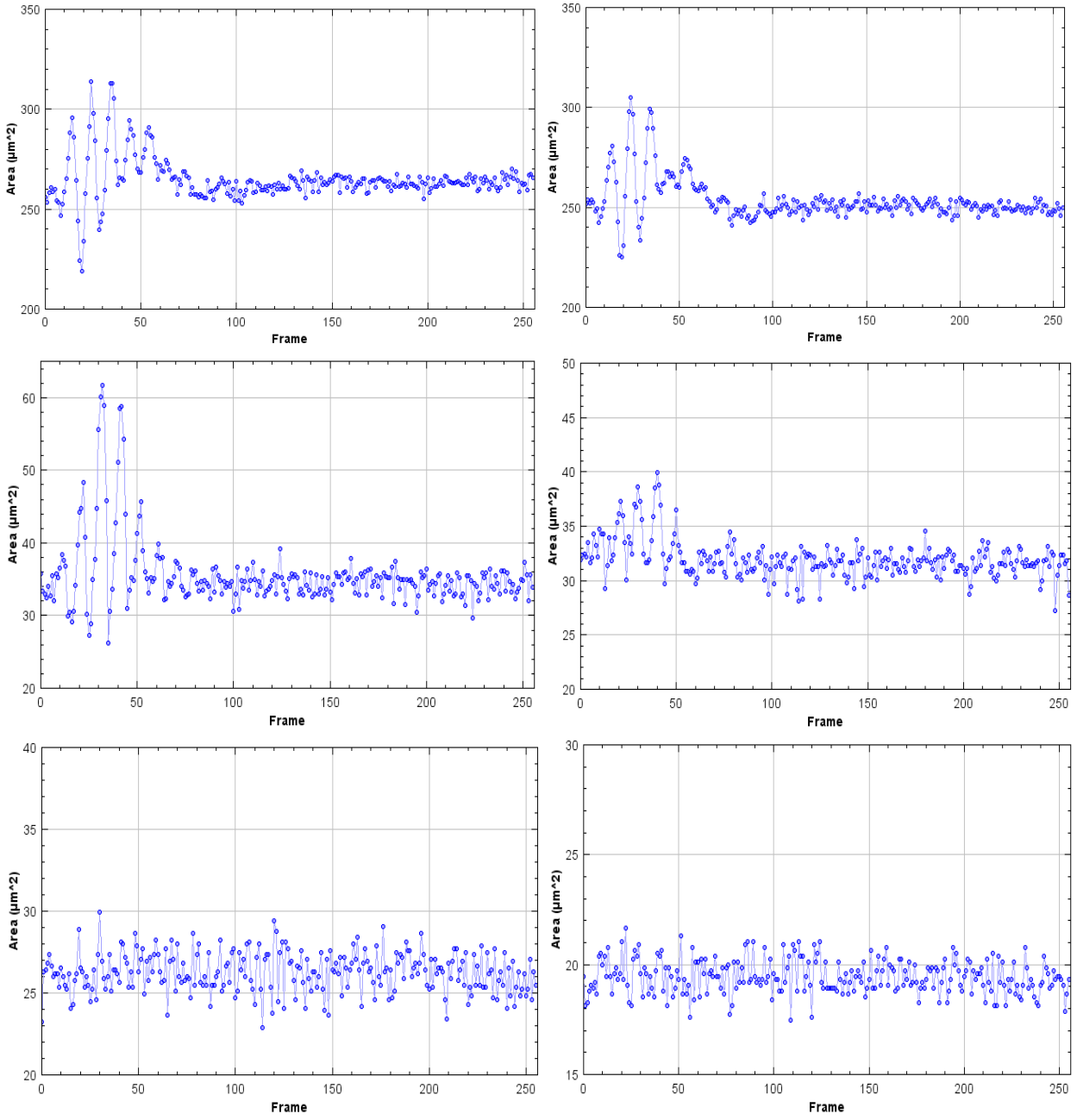

Figure 4.4 Individual size distribution of selected antibubbles under 0.2 MPa where Antibubble1 with Ai= 256.111µm^2 (top-left), Antibubble 2 with 247.701µm^2 (top-right), Antibubble 3 with Ai=35.742 µm^2 (middle-left), Antibubble 4 with Ai=31.932µm^2 (middle-right), Antibubble 5 with Ai=23.259 µm^2 (bottom-left), and Antibubble 6 with Ai=19.448 µm^2 (bottom-right).

Figure 4.4 presents individual size distribution for the selected six antibubbles under three cycles of ultrasonic pulse having 1V amplitude (PNP of 0.2 MPa). Under similar ultrasonic pressure, the size disribution of another six selected antibubbles with different initial area is ploted in one graph for the whole 256 frames in Figure 4.5 to show the rliability and satbility of the size distribution pattern.

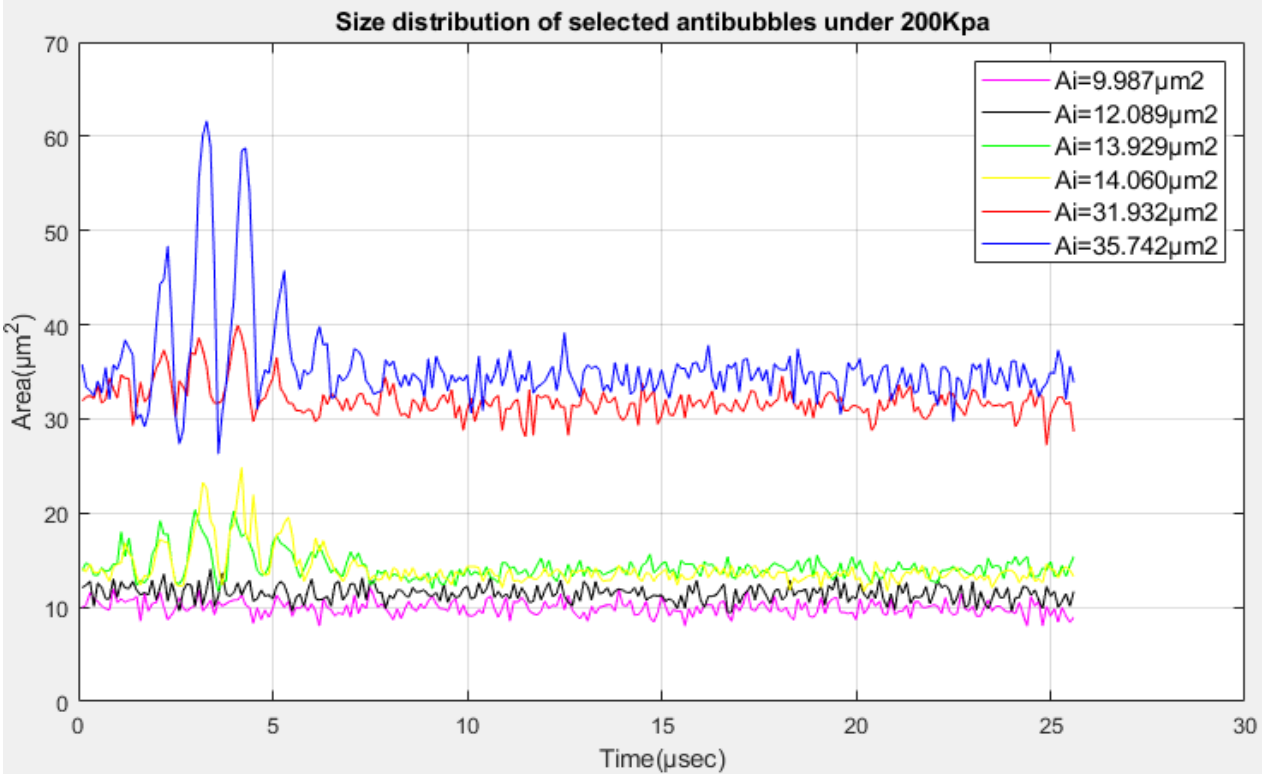

Figure 4.5 Area-time curves of selected antibubbles used to investigate the reliability and stability of their size distribution throughout the whole 256 frames under low acoustic pressure of 0.2 MPa.

As presented in Figure 4.5, the antibubbles show stable oscillation during sonication under three cycles of low pressure ultrasound pulse (also refer Appendix III). This validates the theory related to antibubble responses under low pressure ultrasound pulse which is explained in Chapter 2 (section 2.2.4). It tells that antibubbles oscillate repeatedly with series of stable contraction and expansion when they are subjected to low pressure ultrasound pulse but will not undergo fragmentation. Such type of oscillation is known as stable oscillation. It also matches the size distribution pattern of standard antibubbles under low acoustic amplitude of 0.2 MPa which was presented in terms of radius- time curve in Figure 3.10. This result also validates the

Rayleigh-Plesset equation of antibubble dynamics (Equation 2.2) which suggests that antibubbles expansion increases with their initial size. As could be seen on Figure 4.5, those antibubbles with relatively larger initial size (for example antibubble 1 and antibubble 2 with Ai= 35.742μm^2 and Ai = 31.932μm^2, respectively) show larger expansion than the smaller antibubbles.

Size Distribution under 0.4 MPa Ultrasonic Pressure

The second analysis was made on the response of antibubbles under ultrasound pulse having 2V amplitude (PNP of 0.4 MPa). Figure 4.6 presents a sample microscopic image containing antibubbles segmented using the proposed algorithm and five antibubbles manually identified for further size distribution analysis.

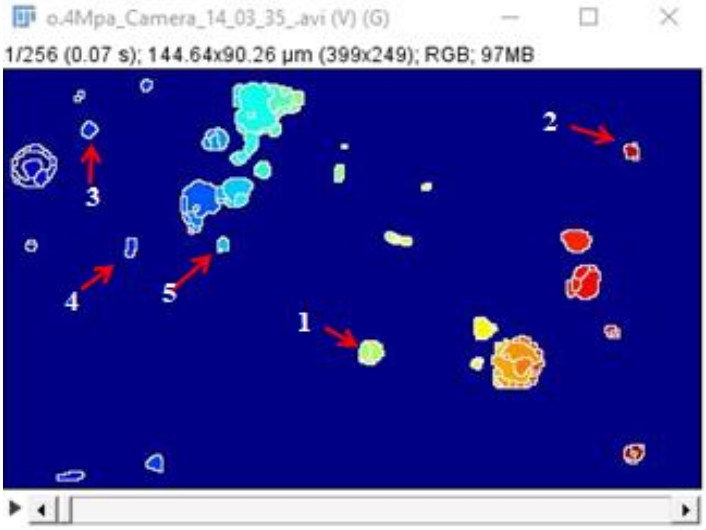

Figure 4.6 Segmented video footage of antibubbles under sonication of 0.4 MPa with five manually identified antibubbles.

Similar to the first experiment, the size distribution for each labeled antibubble is analyzed individually as shown in Figure 4.7.

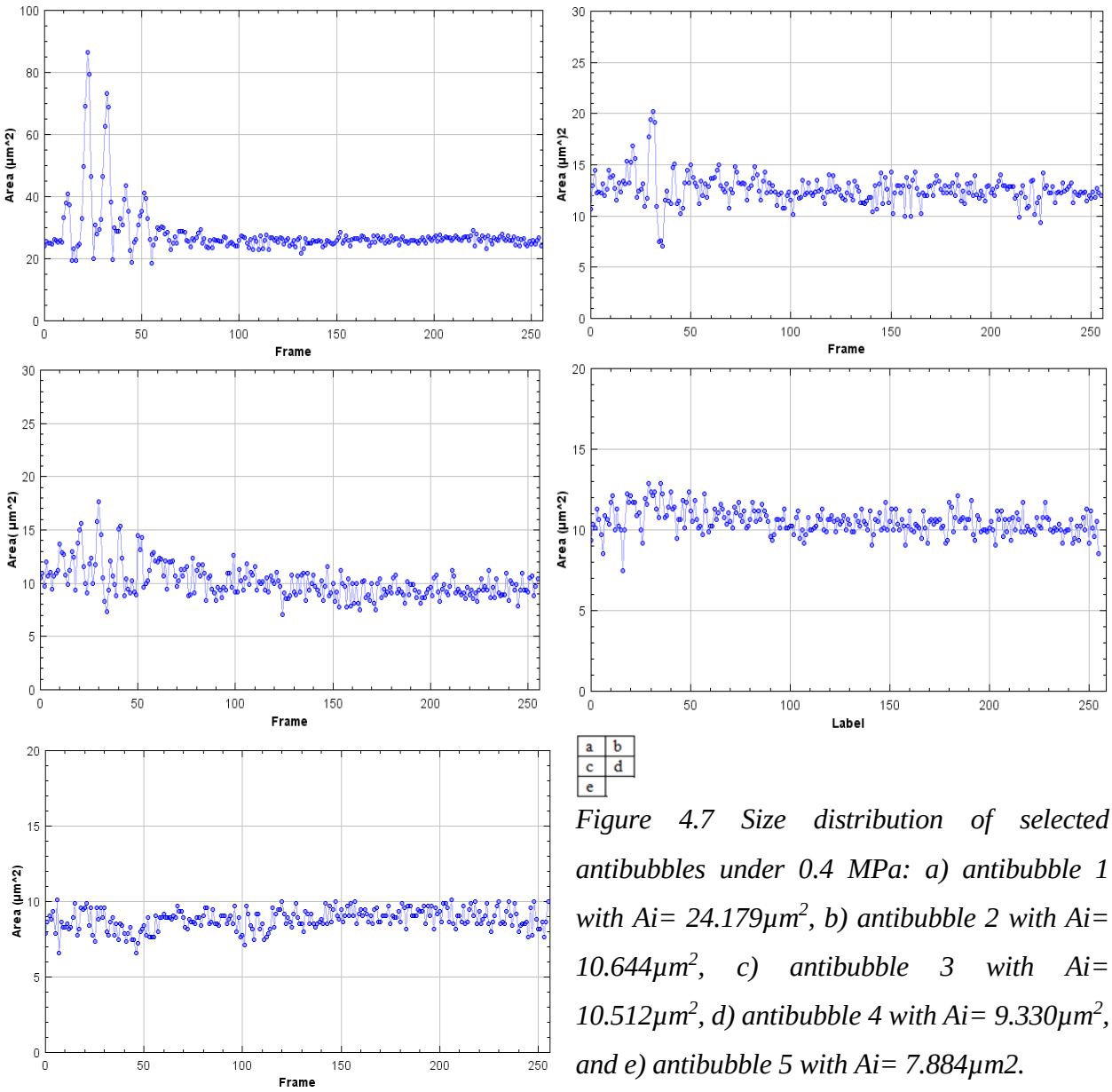

a b
c d
e

Figure 4.7 Size distribution of selected antibubbles under 0.4 MPa: a) antibubble 1 with Ai= 24.179µm^2, b) antibubble 2 with Ai= 10.644µm^2, c) antibubble 3 with Ai= 10.512µm^2, d) antibubble 4 with Ai= 9.330µm^2, and e) antibubble 5 with Ai= 7.884µm2.

The size disribution of the five selected antibubbles is ploted in one graph for the whole 256 frames in Figure 4.8. Like in the case of 0.2 MPa ultrasound pressure, the antibubbles response to 0.4 MPa pulse showed stable oscillation property (also refer Appendix III). The results again validate the theory related to antibubble response under low pressure ultrasound pulse explained in Chapter 2 (section 2.2.4). The major difference between the size distribution of the antibubbles under ultrasound pulse pressure of 0.2 MPa and 0.4 MPa is that in the latter case, the oscillation is relatively higher and more asymmetric. This result once again validates the Rayleigh-Plesset equation of antibubble dynamics which suggests that antibubbles expansion

increases with their initial size. The higher the initial size of the antibubble, the more expansion it shows under low ultrasonic pulse.

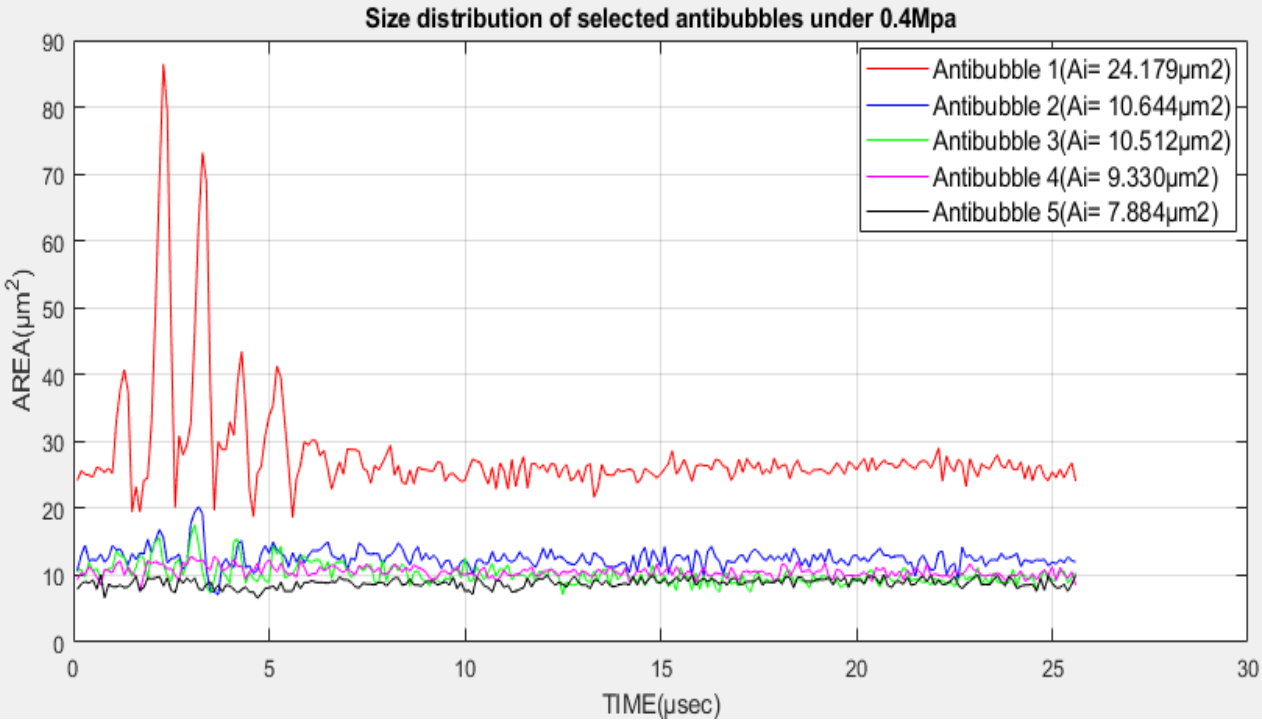

Figure 4.8 Area-time curves of selected antibubbles used to investigate the reliability and stability of their size distribution throughout the whole 256 frames under low acoustic pressure of 0.4 MPa.

For comparison, Figure 4.9 presenst the oscillation patterns of four antibubbles under 0.2 MPa ultrasonic pressure and that of another four antibubbles (with equivalnet intitial sizes) under 0.4 MPa ultrasonic pressure. The figure clearly shows the more asymetric nature of the radial excursion of the antibubbles when under 0.4 MPa pulse compared with that when under 0.2 MPa.

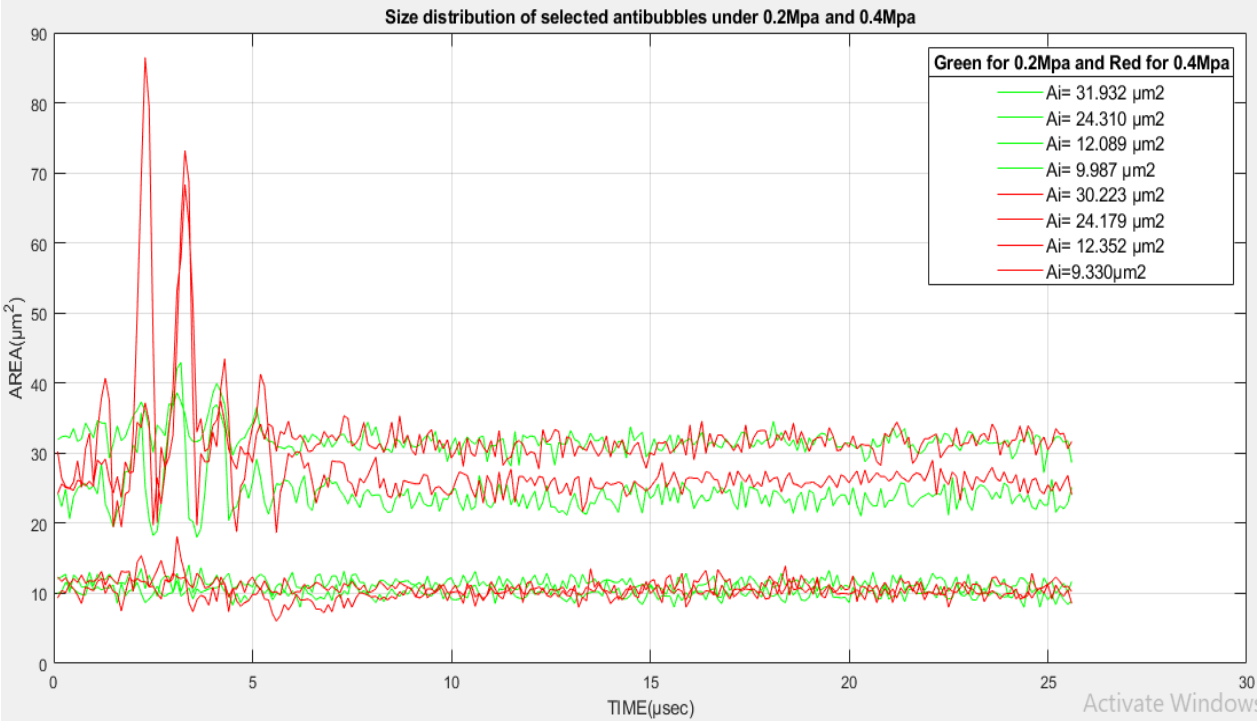

Figure 4.9 Size distribution of four antibubbles under 0.2 MPa ultrasonic pressure (green) and another four equivalent sized antibubbles under 0.4 MPa (red), showing more asymetric radial excursion.

Size Distribution under 0.6 MPa Ultrasonic Pressure

Next, analysis was made on the response of antibubbles under ultrasound pulse having 3V amplitude (PNP of 0.6 MPa). Figure 4.10 presents a sample microscopic image containing antibubbles segmented using the proposed algorithm. Six antibubbles were manually identified on the segmented image for further size distribution analysis and follow-up throughout the three cycles of ultrasound pulse, which was executed per image frame. In this case, the area-time curve was plotted only for the first 40 frames which correspond to 4 µs time duration. The first 40 frames were selected since it is enough to show the oscillation (response) of the antibubbles during the 3 cycles of sonication under high ultrasonic pressure (0.6 MPa). They also experience unstable oscillations which can no longer be followed. Labeling the antibubbles makes it easier to follow their size distribution even if different phenomena such as fragmentation and coalescence could be observed as a result of increased ultrasonic pressure.

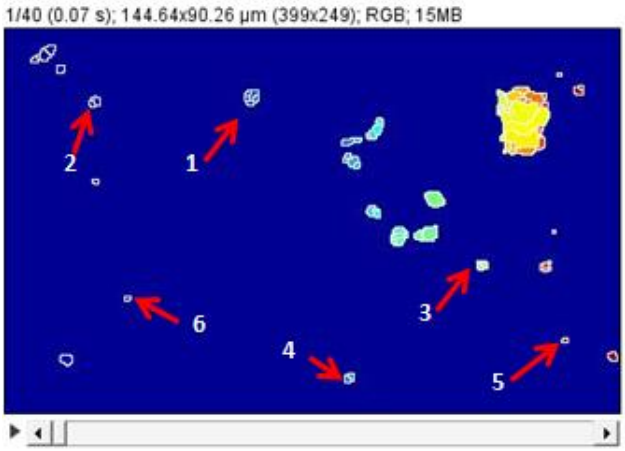

Figure 4.10 Segmented video footage of antibubbles under sonication of 0.6 MPa with six manually identified antibubbles.

The response of all identified antibubbles under three cycles of 0.6 MPa ultrasound pulse with different initial size were analyzed as follows.

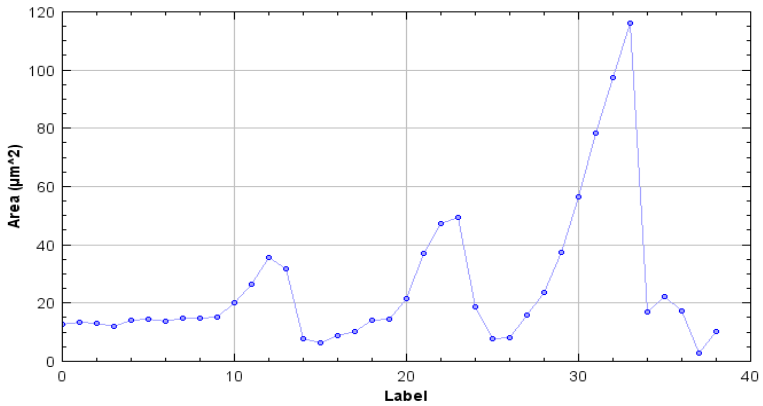

Figure 4.11 Size distribution of antibubble 1 (and coalesced fragments) under three cycles of 0.6 MPa ultrasound pulse with initial size Ai=12.620 µm^2.

Figure 4.11 shows three expansions, all leading to fragmentation of three different antibubbles during the three cycles of sonication, where the first is antibubble 1. This is due to the nature of antibubbles under higher ultrasound pulse which makes them to have higher harmonics and results in merging of nearby antibubbles. This phenomenon is well illustrated in Figure 4.12 where antibubble 1 with initial size of 12.620 µm^2 (labeled as 1) showed maximum expansion during the first cycle of ultrasound pulse with Amax = 35.480 µm^2 (labeled as 13). Then following the maximum expansion, fragmentation during collapse of the antibubble is observed. After fragmentation, again the fragments coalesced (merge) each other forming an entirely new

antibubble with initial area of 21.419 μm^2 (labeled as 21) which again shows maximum expansion during the second cycle of sonication with Amax= 49.540 μm^2 (labeled as 24) followed by fragmentation. Following this second fragmentation, coalesced fragments form a third antibubble having initial area of 56.373 μm^2 (labeled as 31). Finally, in the third cycle of sonication, the antibubble collapses and fragments at a maximum expansion area of 116.032 µm2 (labeled as 34) and with no further sonication afterwards.

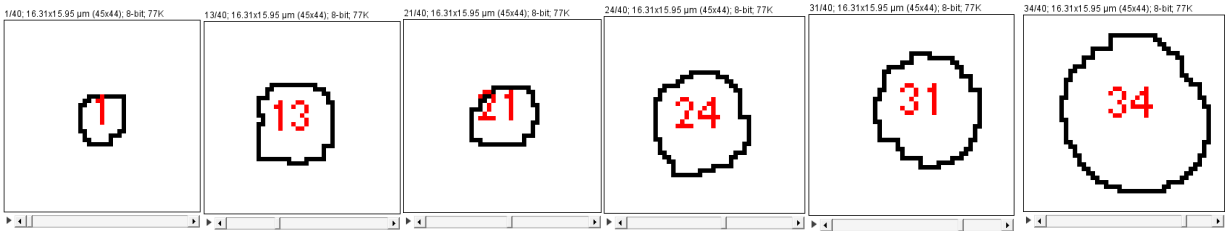

Figure 4.12 Labeled antibubbles during the three cycles of sonication with initial and maximum area.

Similar analysis was made on all identified antibubbles with their initial size and maximum expansion areas which lead to fragmentation under 0.6 MPa ultrasound pulse.

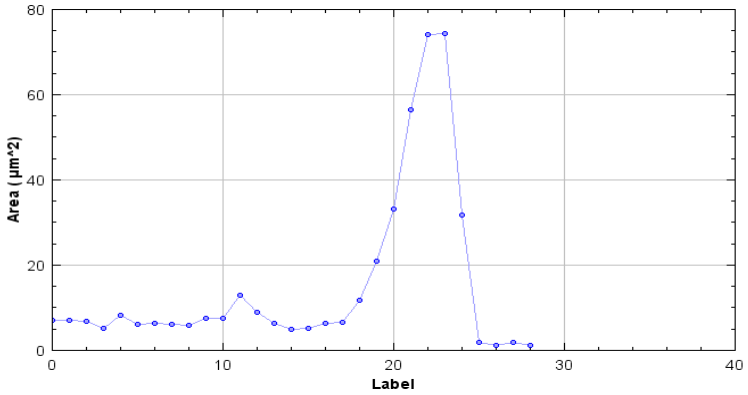

Figure 4.13 Size distribution of antibubble 2 (and coalesced fragments) under three cycles of 0.6 MPa ultrasound pulse with initial size Ai=6.965µm^2.

Figure 4.13 shows size distribution of antibubble 2 and coalesced fragments under 0.6 MPa ultrasound pulse with initial size of Ai=6.965µm^2. It shows maximum expansion during the first cycle of ultrasound pulse with Amax = 12.878 μm^2. Then following the maximum expansion, fragmentation during the collapse of the antibubble is observed. After fragmentation, again the coalesced fragments form a new antibubble with initial area of 33.114 μm^2 which again showed

a maximum expansion during the second cycle of sonication with Amax= 74.376µm^2 followed by fragmentation. No further phenomenon was observed in the third cycle.

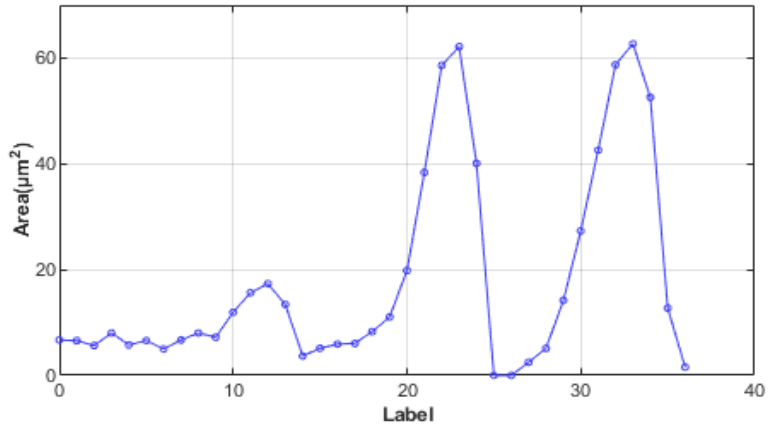

Figure 4.14 Size distribution of antibubble 3 (and coalesced fragments) under three cycles of 0.6 MPa ultrasound pulse with initial size Ai=6.702µm^2.

Figure 4.14 shows size distribution of antibubble 3 and coalesced fragments under 0.6 MPa ultrasound pulse with initial size Ai= 6.702 µm^2. It shows maximum expansion during the first cycle of ultrasound pulse with Amax = 17.346 µm^2. Then following the maximum expansion, fragmentation during the collapse of the antibubble is observed. After fragmentation, again the coalesced fragments form a new antibubble with initial area of 19.842 µm^2 which again showed maximum expansion during the second cycle of sonication with Amax= 40.079 µm^2 followed by fragmentation. Following the second cycle, coalesced fragments form another antibubble having initial area of 27.332 µm^2. Finally, in the third cycle of sonication, the antibubble collapses and fragments at a maximum expansion area of 62.681 µm^2 with no further sonication afterwards.

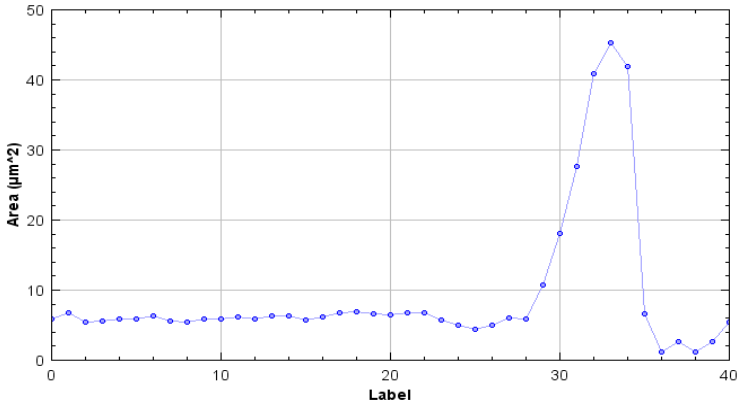

Figure 4.15 Size distribution of antibubble 4 (and coalesced fragments) under three cycles of 0.6 MPa ultrasound pulse with initial size Ai= 5.913 µm^2.

Figure 4.15 shows size distribution of antibubble 4 and coalesced fragments under three cycles of 0.6 MPa ultrasound pulse with initial size Ai= 5.913 μm^2. In this case, no fragmentation was observed during the first and second cycles otherthan stable oscillations. Following the second cycle of sonication, new antibubble was formed as a result of coalesced fragments with initial area of 18.134 μm^2. During the third cycle, this antibubble showed maximum expansion at Amax= 45.335 μm^2 which finally lead to collaps and framentation.

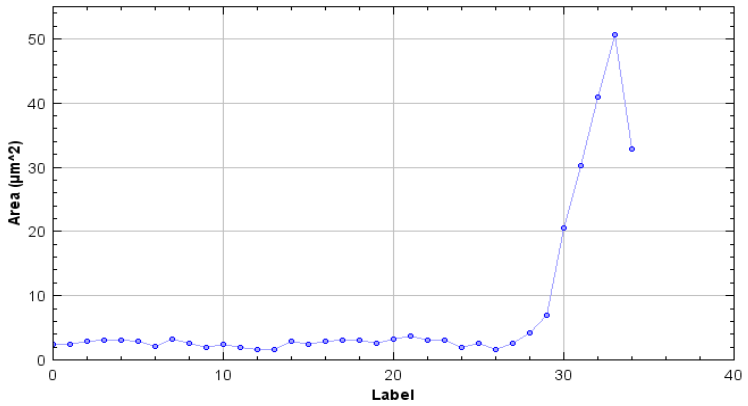

Figure 4.16 Size distribution of antibubble 5 (and coalesced fragments) under three cycles of 0.6 MPa ultrasound pulse with initial size Ai= 2.497 μm^2.

Figure 4.16 presents size distribution of antibubble 5 and coalesced fragments under three cycles of 0.6 MPa ultrasound pulse with initial size Ai= 2.497 μm^2. Similar to antibubble 4, antibubble 5 didn't undergo fragmentation during the first and the second cycles. But after the second cycle of sonication, a new antibubble with initial area 20.499 μm^2 was formed, which expanded to maximum area of 50.591 μm^2 during the third cycle and which finally lead to fragmentation.

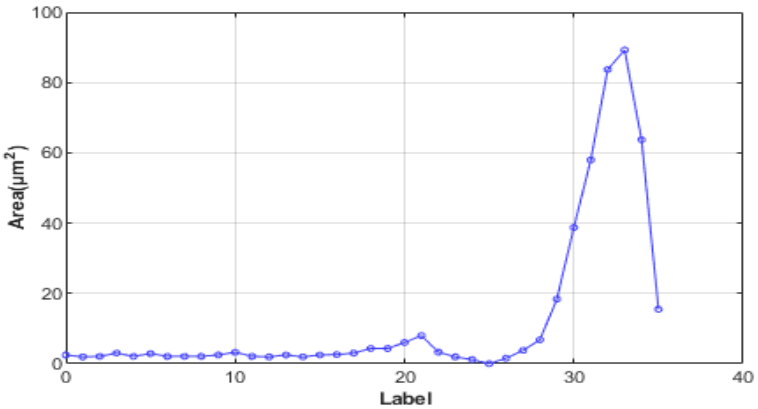

Figure 4.17 Size distribution of antibubble 6 (and coalesced fragments) under three cycles of 0.6 MPa ultrasound pulse with initial size Ai= 2.497μm^2.

Figure 4.17 presents size distribution of antibubble 6 and coalesced fragments under three cycles of 0.6 MPa ultrasound pulse with initial size Ai= 2.497 μm^2. Again, similar to antibubbles 4 and 5, antibubble 6 didn't undergo fragmentation during the first cycle. But after the first cycle of sonication, a new antibubble with initial area of 4.738 μm^2 was formed which then expanded during the second cycle with maximum area of 6.045 μm^2. The coalesced fragments after fragmentation merging with nearby antibubbles formed a new antibubble with initial area of 38.765 μm^2 which then showed a maximum expansion during the third cycle of sonication with Amax= 89.225μm^2 leading to another fragmentation.

Size Distribution under 1.0 MPa Ultrasonic Pressure

The last analysis was made on the response of antibubbles under ultrasound pulse having 5V amplitude (PNP of 1.0 MPa). Figure 4.18 presents a sample microscopic image containing antibubbles segmented using the proposed algorithm. Four antibubbles were manually identified on the segmented image for further size quantification and follow-up throughout the three cycles of ultrasound pulse, which was executed per image frame. Similar to the third analysis, only the antibubbles found on the first 40 frames were labeled and analyzed.

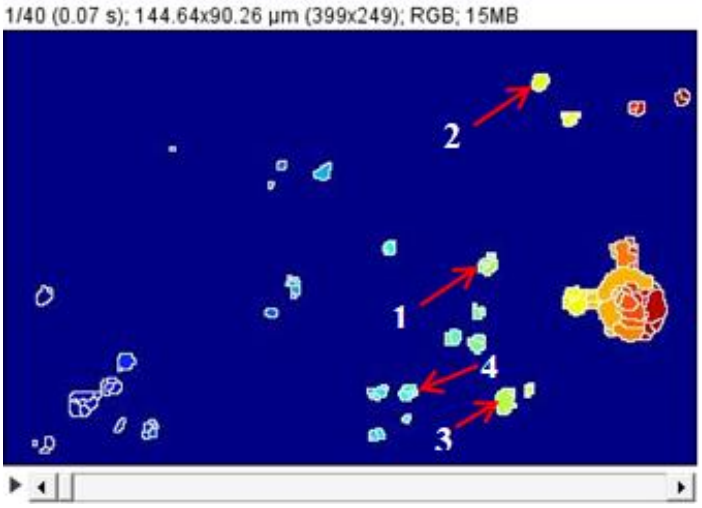

Figure 4.18 Segmented video footage of antibubbles under sonication of 1MPa with four manually identified antibubbles.

The response of all identified antibubbles under three cycles of 1.0 MPa ultrasound pulse with different initial size were analyzed as follows.

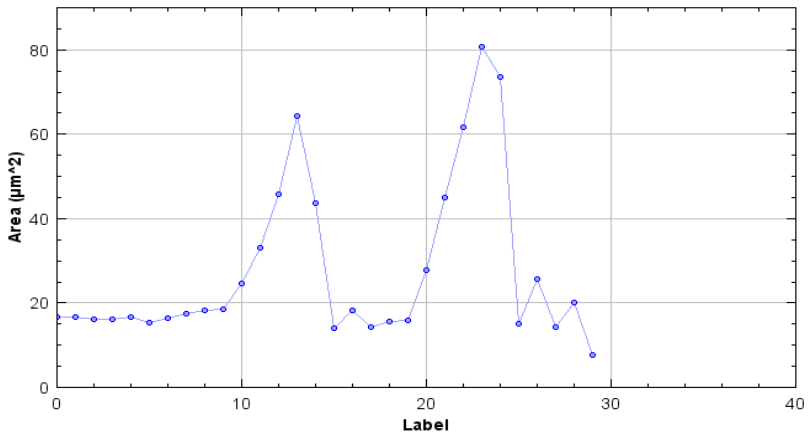

Figure 4.19 Size distribution of antibubble 1 (and coalesced fragments) under three cycles of 1 MPa ultrasound pulse with initial size A_i = 16.557µm^2.

Figure 4.19 shows two expansions, both leading to fragmentation of two different antibubbles during the three cycles of sonication, where the first is antibubble 1. Again, under higher ultrasound pulse, antibubbles experience higher harmonics and that results in merging of nearby fragmented antibubbles. Figure 4.20 illustrates this phenomenon where antibubble 1 and coalesced fragments under 1.0 MPa ultrasound pulse with initial size of 16.557 µm^2 (labeled as 1) showed the first maximum expansion during the first cycle at A_{max} = 64.258µm^2 (labeled as 14). Following the maximum expansion, fragmentation during collapse of the antibubble is observed. After fragmentation, again the coalesced fragment with initial area of 27.727 µm^2 (labeled as 16) showed maximum expansion during the second cycle of sonication at Amax= 80.683µm^2 (labeled as 25). Finally the antibubble collapsed following the maximum expansion after the second cycle and fragments will remain (labeled as 29 and 30). No further phenomenon was observed during the third cycle.

Figure 4.20 Labeled antibubbles under three cycles of ultrasound pulse of amplitude 5V (PNP of 1 MPa).

Similarly, all other identified antibubbles were labeled and analyzed to get their size distribution.

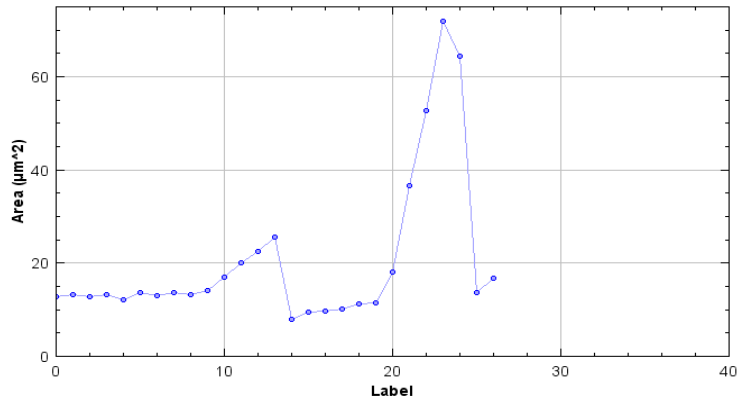

Figure 4.21 Size distribution of antibubble 2 (and coalesced fragments) under three cycles of 1 MPa ultrasound pulse with initial size A_i = 12.746 µm^2.

Figure 4.21 shows size distribution curve of antibubble 2 and coalesced fragments under three cycles of ultrasound pulse with amplitude of 5V (PNP of 1 MPa). The initial size of antibubble 2 was 12.746 µm^2 and showed maximum expansion during the first cycle of ultrasound pulse with A_{max} = 25.624 µm^2. Following the maximum expansion, fragmentation during collapse of the antibubble is observed. After fragmentation, again the coalesced fragment with initial area 18.303 µm^2 showed maximum expansion during the second cycle of sonication at Amax= 71.870 µm^2. Finally, the antibubble collapsed following the maximum expansion after the second cycle and fragments remain.

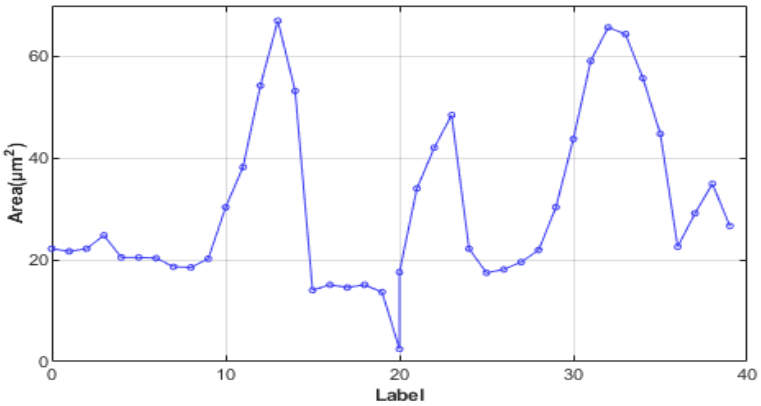

Figure 4.22 Size distribution of antibubble 3 (and coalesced fragments) under three cycles of 1 MPa ultrasound pulse with initial size Ai = 22.208 µm^2.

Figure 4.22 shows the oscillation of antibubble 3 under high acoustic pressure of 1Mpa, where the initial size before the first cycle of sonication was 22.208 µm^2 and showed maximum

expansion during the first cycle with A_{max} = 67.017 µm^2. Then another antibubble which is formed through merging of nearby antibubbles with initial area of 17.608 µm^2 expanded to 48.489 µm^2 during the second cycle which led to another fragmentation. Finally, during the third cycle, the antibubble with initial area 21.945 µm^2 expanded to 65.703 µm^2 and got fragmented.

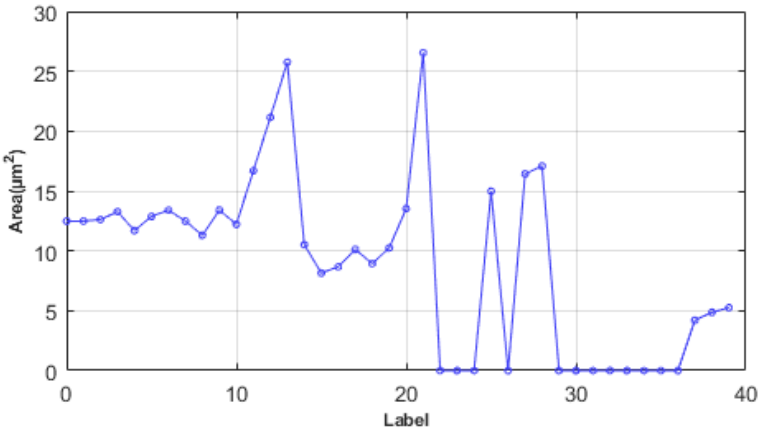

Figure 4.23 Size distribution of antibubble 4 (and coalesced fragments) under three cycles of 1 MPa ultrasound pulse with initial size Ai= 12.484 µm^2.

Figure 4.23 shows the oscillation of antibubble 4 and coalesced fragments under high acoustic pressure of 1MPa, where the initial size before the first cycle of sonication was 12.484 µm^2 and showed maximum expansion during the first cycle with A_{max} = 25.756 µm^2. Another antibubble formed through merging of nearby antibubbles with initial area of 13.535 µm^2 expanded to 26.544µm^2 during the second cycle which led to another fragmentation. No further fragmentation was observed during the third cycle other than oscillation of fragments.

4.3 Destruction Threshold Determination

Size distribution of total of 57 selected antibubbles under ultrasound pulse with acoustic amplitude of 3V and 5V (PNP of 0.6 MPa and 1 MPa respectively) were analyzed to determine the destruction threshold of antibubbles intermes of their expected maximum expansion with respect to their initial size. Out of the 57 antibubbles, 29 were subjected to 0.6 MPa and 28 were subjected to 1 MPa ultrasonic pressures (Refer Appendix III).

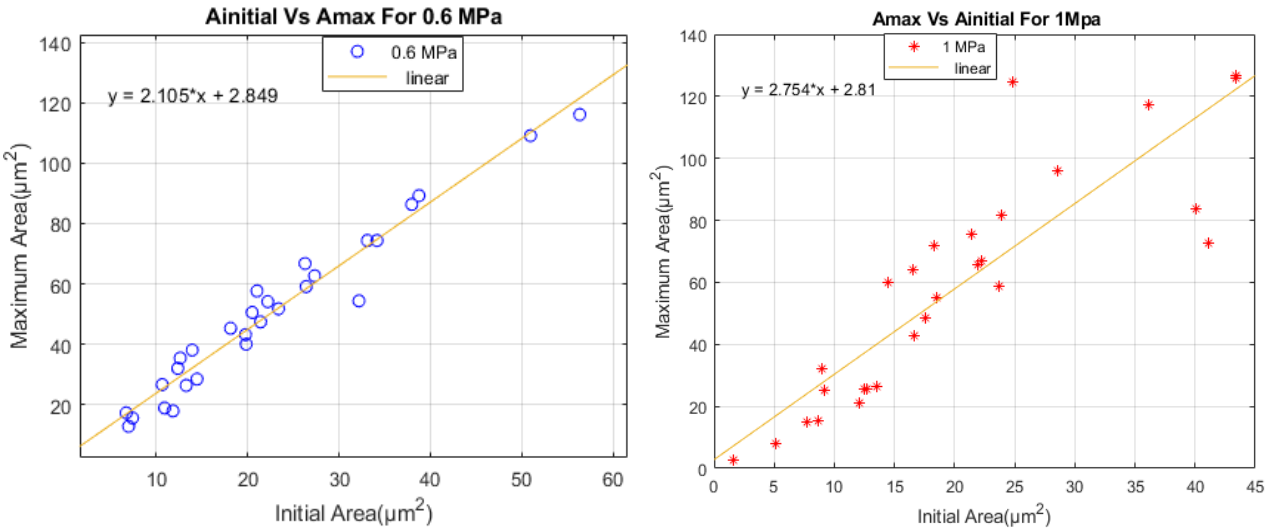

Figure 4.24 Antibubbles maximum area of expansion versus their initial area (left) for 0.6MPa and (right) for 1MPa ultrasonic pressures.

Figure 4.24 shows the relationship between the maximum area of expansion of antibubbles (which leads to fragmentation) and their initial area when subjected to ultrasound pulse having 0.6Mpa and 1Mpa ultrasonic pressures. The Figure clearly showed a linear relationship between the maximum area of expansion with that of the initial area of the antibubbles. A more linear correlation is observed in the case of 0.6 MPa pulses compared to 1 MPa where there were few outliers. The oscillation pattern of the antibubbles gets more asymmetric with relatively higher positive excursion at 1 MPa compared to 0.6 MPa. This once again validates the Rayleigh-Plesset equation (2.2) which states that increase in amplitude of applied ultrasound results in more asymmetric radial excursion. It also suggests that antibubbles expansion depends on their initial size in addition to the applied ultrasonic pressure which is again validated here using the experimental data. The second governing theory of fragmentation is parametric instability. It is caused by shape instability which is the result of radial oscillation (expansion and contractions). As the experimental results show, when antibubbles are subjected to higher ultrasonic pressures, they experience higher order spherical harmonic oscillation which is the source for their instability and result in fragmentation. Sufficiently big expansion concentrates enough energy to break apart the antibubbles as hypothesized based on the theory.

Basic curve fitting shows the linear relation between maximum expansion and initial size for both 0.6 MPa and 1 MPa as shown in Figure 4.24. From the linear relationship, Amax ≈ 2.1Ai for 0.6 MPa and Amax ≈ 2.75Ai for 1MPa which could be compared with the Blake threshold

approximation. Hence, the destruction threshold was re-computed in terms of maximum radius of expansion of the antibubbles and initial radii for both high ultrasonic pressures of 0.6 MPa and 1 MPa. The relationship between the two is depicted in Figure 4.25. According to Blake threshold approximation, the initial and the maximum radius of expansion are related linearly as $R_{cr} \approx 2R_i$. To compare with that of Blake's approximation, the initial and maximum area of expansion were used in the current study to compute the corresponding radii assuming antibubbles are spherical (circular in 2D) in shape (i.e.$R = \sqrt{(Area / \pi)}$). This assumption is known to be far from the actual as antibubbles show more non-spherical (more irregular) shape patterns particularly when they are under sonication. From the linear relationship, Rmax ≈ 1.453Ri for 0.6 MPa and Rmax ≈ 1.787Ri for 1MPa computed based on simple curve fitting.

Comparing the Blake threshold approximation for antibubbles fragmentation with the real experimental results, discrepancies are observed. The experimental findings showed that Rmax/R0≪2 (around 1.5 for 0.6 MPa and 1.8 for 1 MPa) as also could be seen on Figure 4.25. As also mentioned in Chapter 2 (section 2.2.4), previous studies carried out on microbubbles fragmentation reported that Rmax/R0≪2, in good agreement with the results presented in the current study [8]. This, however, contradicts Blake critical radius approximation.

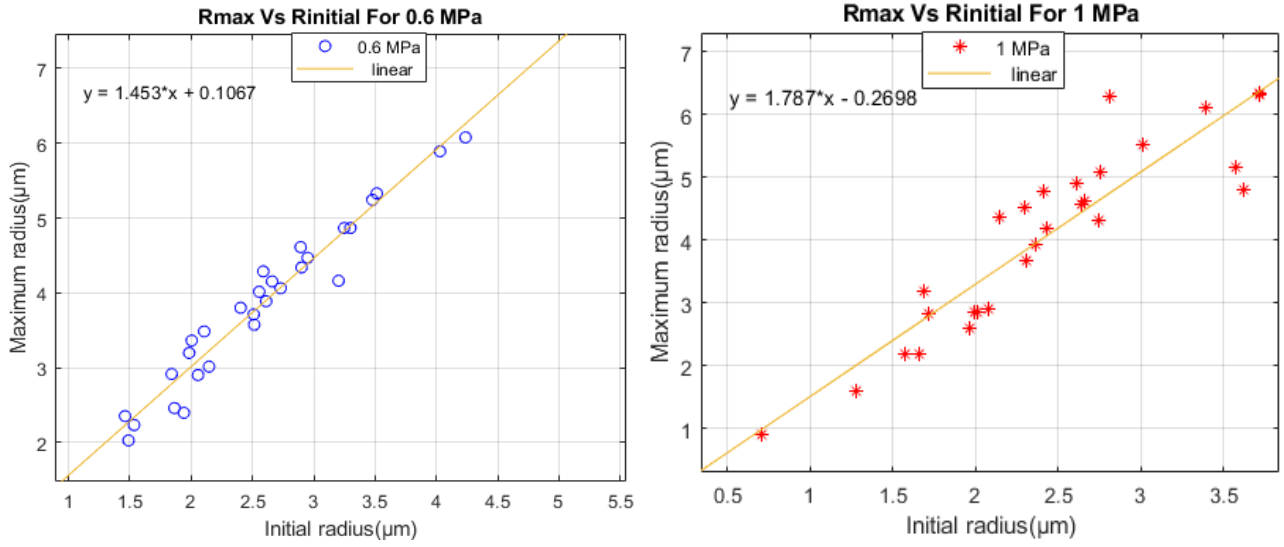

Figure 4.25 Antibubbles maximum radius of expansion versus their initial radius (left) for 0.6MPa and (right) for 1MPa ultrasonic pressures.

Chapter 5: Conclusion and Recommendation

5.1 Conclusion

Detecting an antibubble was the major part of this research in order to be able to make further analysis including size measurement and destruction threshold determination. The proposed algorithm that involved local GLCM feature extraction and watershed segmentation preceded by useful preprocessing tools showed promising results in segmenting antibubbles with a clear boundary. The size distribution patterns also show the effectiveness of the segmentation scheme.

The investigation on size distribution of antibubbles under sonication of low pressure ultrasound waves showed that antibubbles oscillate repeatedly with series of stable contractions and expansions but will not undergo fragmentation, the so called stable oscillation. This property of antibubbles interaction with low pressure ultrasound waves makes them very useful and preferable to be used as a drug carrier in a way of manipulating the antibubble movement through the blood vessels to the target region. In case of antibubble sonication under higher acoustic pressure waves, their oscillations become more asymmetric with increased positive excursion which finally leads to fragmentation.

Investigation on the destruction threshold that leads to fragmentation can be applicable and useful in optimization of the ultrasound pulse parameters to use with the antibubbles during drug delivery within the safest MI. The purpose of this investigation was to determine the destruction threshold of antibubbles intermes of their maximum area of expansion given their initial size. The results showed that antibubbles under acoustic pressure of 0.6 MPa experience fragmentation when their size during maximum expansion is approximately twice that of their initial size, i.e. $A_{max} \approx 2.1\ A_{i.}$ In the case of 1 MPa acoustic pressure, $A_{max} \approx 2.8\ A_i$, showing that under 1 MPa, antibubbles experience more inertial cavitation than at 0.6 MPa. Similar experimental analysis carried out using the radius of the antibubbles showed that $R_{max}/R_o \ll 2$ indicating Blake threshold approximation is not necessarily a good approximation.

Safety is one of the greatest requirements during ultrasound targeted drug delivery since the process might cause harmful bio-effects if the cavitation is out of safe MI range. The recommended upper bound value for MI is about 0.7 above which significant risks of cavitation can be observed. Even though the lowest acoustic amplitudes are within the safest MI range, they

are not sufficient enough to cause fragmentation. On the other hand, the higher acoustic amplitudes, 0.6 MPa and 1 MPa, can lead to sufficiently big expansion of antibubbles, which concentrates enough energy to destruct them. Ultrasound pulse with acoustic pressure of 0.6 MPa is considered safe compared to 1 MPa for use in drug delivery with the capacity to induce fragmentation and effective targeted drug release.

5.2 Recommendation

Testing the proposed size determination and destruction threshold scheme on bigger data set could reveal its potentials for use in effective drug delivery of the antibubbles. Feature selection, used during image segmentation, was entirely based on qualitative assessment while other methodologies could be devised including use of artificial intelligence (AI) to do so. This might also help to take into account the effect of the size and number of core droplets inside the antibubbles. This is as opposed to just considering the entire antibubble as one composed of core droplet/s and gaseous shell. One other interesting aspect while trying to understand antibubble properties under sonication is the effect of pulse repetition, where its effect is omitted in the current study. Such and similar other issues require much more investigation.

References

[1] N. Martinho, C. Damge, C. P. Reis, "Recent Advances in Drug Delivery Systems," *Journal of Biomaterials and Nano biotechnology,* vol. 2, no. 5, pp. 510-526, 2011.

[2] S. Hernot and A. L. Klibanov, "Microbubbles in ultrasound-triggered drug and gene delivery," *Advanced drug delivery reviews,* vol. 60, no. 10, p. 1153–1166, June 2008.

[3] S. Kotopoulis, and A. Delalande, M. Popa, V. Mamaeva, G. Dimcevski, O. H. Gilja, M. Postema, B. T. Gjertsen, E. McCormac, "Sonoporation-enhanced chemotherapy significantly reduces primary tumour burden in an orthotopic pancreatic cancer xenograft," *Molecular Imaging and Biology,* vol. 16, no. 1, pp. 53-62, February 2014.

[4] S. M .Chowdhury, T. lee, J. K. Willmann, "Ultrasound-guided drug delivery in cancer," *Ultrasonography,* vol. 36, no. 3, pp. 171-184, May 2017.

[5] M. Postema, O. H. Gilja, "Ultrasound-directed drug delivery," *Curr Pharm Biotechnol,* vol. 8, no. 6, p. 355–361, November 2007.

[6] L.J. Delaney, S. Isguven, J.R. Eisenbrey, N.J. Hickok, F. Forsberg, "Making Waves: how ultrasound targeted drug delivery is changing pharmaceutical approaches," *Materials Advances,* vol. 3, no. 7, pp. 3023-3040, February 2022.

[7] G. A Husseini, M.A . Diaz de la Rosa, E. S. Richardson, D.A. Christensen,W.G. Pitt, "The role of cavitation in acoustically activated drug delivery," *J Control Release,* vol. 107, no. 2, pp. 253-261, October 2005.

[8] M. Postema,G. Schmitz, " Ultrasonic fragmentation of microbubbles: a theoretical approach of the flash in flash-echo," *IEEE,* pp. 1-4, 2005.

[9] M. Postema, G. Schmit, "Ultrasonic bubbles in medicine: Influence of the shell," *Ultrasonics Sonochemistry,* vol. 14, no. 4, p. 438–444, 2007.

[10] R. Suzuki, T. Takizawa, Y. Negishi, K. Hagisawa, K. Tanaka, K. Sawamura, N. Utoguchi, T. Nishioka, K. Maruyama, "Gene delivery by combination of novel liposomal bubbles with perfluoropropane and ultrasound," *J Control Release,* vol. 117, no. 1, pp. 130-136, 2007.

[11] M. postema, F.J ten Cate, G. Schmitz, N.d. Jong, A.Van, "Generation of droplet inside a microbble with the aid of an ultrasound contrast agent: First result," *Drug Design and Discovery,* vol. 4, no. 1, pp. 74-77, 2007.

[12] A. T. Poortinga, "long-lived antibubbles : Stable antibubbles through pickering stablization," *Langmuir,* vol. 7, no. 6, pp. 2138-2141, January 2011.

[13] J.E. Silpe, J.K. Nunes, A.T. Poortinga, H.A. Stone, "Generation of antibubblrd from core-shell double emulsion templates produced by microfluidics," *Langmuir,* vol. 29, no. 28, pp. 8782-8787, June 2013.

[14] K. Johansen, S. Kotopoulis, O. H. Giljaa, A. T. Poortingad, M. Postema, "Acoustically active antibubbles," *Acta Physica Polonica,* vol. 127, no. 1, pp. 99-102, January 2015.

[15] K. Johansen, S. Kotopoulis, A. T. Poortingad, M. Postema, "Nonlinear Echoes from Encapsulated Antibubbles," *Nonlinear Echoes from Encapsulated Antibubbles,* vol. 70, pp. 1079-1082, August 2015.

[16] M. Postema, A. Novell, C. Sennogaa, A. T. Poortingad, A. Bouakaza, "Harmonic response from microscopic antibubble.," *Applide Acoustics,* vol. 137, pp. 148-150, August 2018.

[17] Y. Vitrya, St. Dorbolo, J. Vermantc and B. Scheid, "Controlling the lifetime of antibubbles," *Advances in Colloid and Interface Science,* vol. 270, pp. 73-86, August 2019.

[18] N.Anderton, "Acoustic Properties of Antibubblea. MSc. dissertation, Department of Engineering and the Built Environment.," Johannesburg, 2019.

[19] S. Kotopoulis, C. Lam, R. Haugse, S. Snipstad, E. Murvold, T. Jouleh, S. Berg, R. Hansen, M. Popa, E.M. Cormack, O.H. Gilja, A. Poortinga, "Formulation and characterisation of drug-loaded antibubbles for image-guided and ultrasound triggered drug delivery," *Ultrason Sonochemistry,* vol. 85, March 2022.

[20] VT Jr. DeVita, E. Chu, "A history of cancer chemotherapy," *Cancer Res,* vol. 68, no. 21, pp. 8643-8653, November 2008.

[21] B. A. Chabner,T. G. Jr. Roberts, " Chemotherapy and the war on cancer," *Nat Rev Cancer,* vol. 5, no. 1, pp. 65-72, January 2005..

[22] M. Postema, S. Kotopoulis, K. Jenerka., Physical Principles of Medical Ultrasound, 2nd ed., London: EFSUMB, 2019, p. 1–23.

[23] Z. Izadifar, P.S. Babyn, D. Chapman, "Application and safety of therapeutic ultrasound: current trends and future potential," *Clinical research open access,* vol. 3, no. 1, January 2017.

[24] A. Murphy, M. Nadrljanski, "Physcal principle of ultrasound," *Radiopaedia,* March 2020.

[25] D. M. Rubin, N. Anderton, C. Smalberger, J. Polliack, M. Nathan, M. Postema, "On the behaviour of living cells under the influence of ultrasound," *Fluids* , vol. 3, no. 82, October 2018.

[26] T. sen, Y. Koza, O. Tufekcioglu, "Mechanical index," *Anatolian Journal of cardiology*, pp. 334-336, April 2015.

[27] Society, Prepared by the Safety Group of the British Medical Ultrasound, "Guidelines for the safe use of diagnostic ultrasoundequipment," *Ultrasound,* vol. 18, no. 2, p. 52–59, May 2010.

[28] N. Mazzawi, M. Postema, E. Kimmel, "Bubble-like response of living blood cells in an ultrasound field," *Acousto-Optics and Applications,* vol. 127, no. 1, January 2015.

[29] T. G. Leighton, "The Acoustic Bubble," *Journal of Fluid Mechanics,* vol. 272 , pp. 407 - 408, August 1994.

[30] M. Postema, Fundamentals of Medical Ultrasonics, 1st ed., Central Academic Complete press, 2014, p. 177–201.

[31] M. Postema, O. H. Gilja, "Contrast-enhanced and targeted ultrasound," *World Journal of Gastroenterology,* vol. 17, no. 1, p. 28–41, January 2011.

[32] W. Hughes, A. R. Hughes, "Liquid Drops on the Same Liquid Surface," *Nature,* vol. 129, no. 59, January 1932.

[33] C. L. Stong, "Curious bubbles in which a gas encloses a liquid instead of the other way around," *Journal of Fluid Mechanics,* vol. 230, pp. 116-120, April 1974.

[34] M. Postema, A. van Wamel, F. J. ten Cate, N. de Jong., "High-speed photography during ultrasound illustrates potential therapeutic applications of microbubbles," *Medical physics,* vol. 32, no. 12, p. 3707–3711, December 2005.

[35] L. Bai, W. Xu, P. Wu, W. Lin, C. Li, D. Xu, "Formation of antibubbles and multilayer antibubbles," *Colloids and Surfaces A: Physicochemical and Engineering Aspects,* vol. 509, p. 334–340, December 2016.

[36] N. Kudo, R. Uzbekov, R. Matsumoto, R. Shimizu, C. Carlson, N. Anderton, A. Deroubaix, C. Penny, A. T. Poortinga, D. M. Rubin, A. Bouakaz, M. Postema, "Asymmetric oscillation of endoskeletal antibubbles," *Japanese Journal of Applied Physics,* vol. 59, no. 2, 2020.

[37] A. T. Poortinga, "Micron-sized antibubbles with tunable stability," *Colloids and Surfaces A:*

Physicochemical and Engineering Aspects, vol. 419, p. 15–20, February 2013.

[38] Y. Du, B. Chen., "Combination of drugs and carriers in drug delivery technology and its development," *Drug Design, development and Therapy,* vol. 13, pp. 1401-1408, April 2019.

[39] J. E. Chomas, P. Dayton, D. May, and K. Ferrara., "Threshold of fragmentation for ultrasonic contrast agents," *Journal of Biomedical Optics,* vol. 6, no. 2, p. 141–150, April 2001.

[40] C. Brennen, Cavitation and bubble Dynamics, Oxford University Press, 1995, pp. 59-62.

[41] O. Marques, Practical image and video processing using MATLAB, Wiley IEEE Press, 2011.

[42] C. Solomon, T. Breckon, Fundamentals of Digital Image Processing: A practical approach with examples in Matlab, John Wiley & Sons, 2011.

[43] G. Yadav, S. Maheshwari, A. Agarwal, "Contrast limited adaptive histogram equalization based enhancement for real time video system," in *International conference on advance in computing, communications and informatics (ICACCI),* 2014.

[44] A. M. Reza, "Realization of the contrast limited adaptive histogram equalization (CLAHE) for real time enhancement," *Journal of VLSI signal processing,* vol. 38, no. 1, pp. 35-44, May 2003.

[45] P. Mohanaiah, P. Sathyanarayana, L. GuruKumar, "Image Texture Feature Extraction Using GLCM Approach," *International Journal of Scientific and Research Publications,* vol. 3, no. 5, May 2013,.

[46] R. M. Haralick, K. Shamumagam, I. Dinstein , "Textural Features of Image Classification," vol. 3, no. 6, pp. 610-621, 1973.

[47] F.Albregtsen, "Statistical Texture Measures Computed from Gray Level Co-occurrence Matrices: Image Processing Laboratory, Department of Informatics," 2008.

[48] K. Dilpreet, K. Yadwinder, "Various Image Segmentation Techniques: A Review," *International Journal of Computer Science and Mobile Computing,* vol. 3, no. 5, p. 809 – 814, May 2014.

[49] M. Singh, "Edge based image segmentation: Major project submitted in partial fulfilment of the requirement for degree of masters," Delhi Technological university, Delhi, 2014.

[50] D. Karungan, N.Sujatha, "Survey on various image segmentation techniques," *Journal of emerging technology and innovative research,* vol. 4, no. 02, pp. 115-120, February 2017.

[51] B. Karthicsonia, M. Vanitha, "Edge based segmentation in medical images," *International Journal of Engineering and Advanced Technology*, vol. 9, no. 1, pp. 449-451, October 2019.

[52] A. Shafi, D. Padha, "Medical Image Segmentation: Review of Recent Techniques, Advancements and a Comprehensive Comparison”," *InternationalJournal of Computer Sciences and Engineering*, vol. 7, no. 7, pp. 114-124, July 2019.

[53] A.E. Allaoui, M.B. Nasir, "Medical image segmentation by marker controlled watershed and mathimatical morphology," *International journal of multimedia and its application (IJMA)*, vol. 4, no. 3, p. 2, June 2012.

[54] A. Bala, "An improved watershed image segmentation technique using matlab," *International journal of scientific and engineering research*, vol. 3, no. 6, June 2012.

Appendix

Appendix I: Matlab Codes

I.I Image Segmentation

```
close all
clear all
clc

vidObj=VideoReader('Camera_14_11_10_AB#1(5mg)_5V_1MPa_3cycles_40times.avi');
Wptr = VideoWriter('1Mpa_Camera_14_11_10_.avi');
Wptr .FrameRate = vidObj.FrameRate;

%Open the output video file
open(Wptr);

for n =1: 256
   vidFrame = readFrame(vidObj);
   I = vidFrame;

% STEP 2:Pre-processing

I1=medfilt2(I,[3,3]);

%apply complement on the original image
  I_C= imcomplement(I1);

% apply contrast-limited adaptive histogram equalization % for contrast adjustment
  I_eqq = adapthisteq(I_C);
  I_eqq = imclearborder(I_eqq);

% Step3: Apply Local GLCM
window_size = 3; %%// window size
wsz = window_size-1;
mp = floor(window_size/2);

img = I_eqq;
for k1= 1:size(img,1)-wsz
   for k2= 1:size(img,2)-wsz
     window_data = img(k1:k1+wsz,k2:k2+wsz);

       offsets = [0 1;-1 1;-1 0;-1 -1;1 1;1 0;1 -1;0 -1];
       [glcms,I_eqglcm] = graycomatrix(window_data,'Offset',offsets);
        out = GLCM_Features2(sum(glcms,3));
```

```
% Features computed

      img9(k1+mp,k2+mp)= out.maxpr;     % Maximum probability
   end
end

 I_glcm=img9;   %max.probability glcm
 I9_glcm_C= imcomplement(I_glcm);

% Step 4: Watershed Segmentation

  L_I1 = watershed(I9_glcm_C);
  Lrgb_I = label2rgb(L_I1);
  writeVideo(Wptr,Lrgb_I);
disp (['Processed Frame:',num2str(n)]);
end
n=n+1;
close(Wptr);

%--------------------------------------------------------------------------
```

%Graycomatrix create gray-level co-occurrence matrix.

```
function [GLCMS,SI] = graycomatrix(varargin)
 [I, Offset, NL, GL, makeSymmetric] = ParseInputs(varargin{:});
if GL(2) == GL(1)
  SI = ones(size(I));
else
    slope = NL / (GL(2) - GL(1));
    intercept = 1 - (slope*(GL(1)));
    SI = floor(imlincomb(slope,I,intercept,'double'));
end
    SI(SI > NL) = NL;
    SI(SI < 1) = 1;
numOffsets = size(Offset,1);
if NL ~= 0
  s = size(I);
  [r,c] = meshgrid(1:s(1),1:s(2));
  r = r(:);
  c = c(:);
```

```
% Compute GLCMS
  GLCMS = zeros(NL,NL,numOffsets);
  for k = 1 : numOffsets
    GLCMS(:,:,k) = computeGLCM(r,c,Offset(k,:),SI,NL);
    if makeSymmetric
       % Reflect glcm across the diagonal
       glcmTranspose = GLCMS(:,:,k).';
       GLCMS(:,:,k) = GLCMS(:,:,k) + glcmTranspose;
    end
  end
else
  GLCMS = zeros(0,0,numOffsets);
end
%---------------------------------------------------------------------------
```

% GLCM_Features2 (Function to calculate GlCM features)

```
function oneGLCM = computeGLCM(r,c,offset,si,nl)
function [out] = GLCM_Features1(glcmin,pairs)
if ((nargin > 2) || (nargin == 0))
   error('Too many or too few input arguments. Enter GLCM and pairs.');
elseif ( (nargin == 2) )
    if ((size(glcmin,1) <= 1) || (size(glcmin,2) <= 1))
       error('The GLCM should be a 2-D or 3-D matrix.');
    elseif ( size(glcmin,1) ~= size(glcmin,2) )
        error('Each GLCM should be square with NumLevels rows and NumLevels cols');
    end
elseif (nargin == 1) % only GLCM is entered
    pairs = 0; % default is numbers and input 1 for percentage
    if ((size(glcmin,1) <= 1) || (size(glcmin,2) <= 1))
       error('The GLCM should be a 2-D or 3-D matrix.');
    elseif ( size(glcmin,1) ~= size(glcmin,2) )
       error('Each GLCM should be square with NumLevels rows and NumLevels cols');
    end
```

```
end
format long e
if (pairs == 1)
   newn = 1;
   for nglcm = 1:2:size(glcmin,3)
      glcm(:,:,newn)  = glcmin(:,:,nglcm) + glcmin(:,:,nglcm+1);
      newn = newn + 1;
   end
elseif (pairs == 0)
   glcm = glcmin;
end
size_glcm_1 = size(glcm,1);
size_glcm_2 = size(glcm,2);
size_glcm_3 = size(glcm,3);
out.maxpr = zeros(1,size_glcm_3); % Maximum probability
u_x = zeros(size_glcm_3,1);
u_y = zeros(size_glcm_3,1);
s_x = zeros(size_glcm_3,1);
s_y = zeros(size_glcm_3,1);
% % alternate values of u and s
% u_x2 = zeros(size_glcm_3,1);
% u_y2 = zeros(size_glcm_3,1);
% s_x2 = zeros(size_glcm_3,1);
% s_y2 = zeros(size_glcm_3,1);
p_x = zeros(size_glcm_1,size_glcm_3); % Ng x #glcms[1]
p_y = zeros(size_glcm_2,size_glcm_3); % Ng x #glcms[1]
p_xplusy = zeros((size_glcm_1*2 - 1),size_glcm_3); %[1]
p_xminusy = zeros((size_glcm_1),size_glcm_3); %[1]
hxy  = zeros(size_glcm_3,1);
hxy1 = zeros(size_glcm_3,1);
hx   = zeros(size_glcm_3,1);
hy   = zeros(size_glcm_3,1);
hxy2 = zeros(size_glcm_3,1);
```

```
for k = 1:size_glcm_3 % number glcms
    glcm_sum(k) = sum(sum(glcm(:,:,k)));
    glcm(:,:,k) = glcm(:,:,k)./glcm_sum(k); % Normalize each glcm
    out.maxpr(k) = max(max(glcm(:,:,k)));
end
% glcms have been normalized:
```

I.II GUI

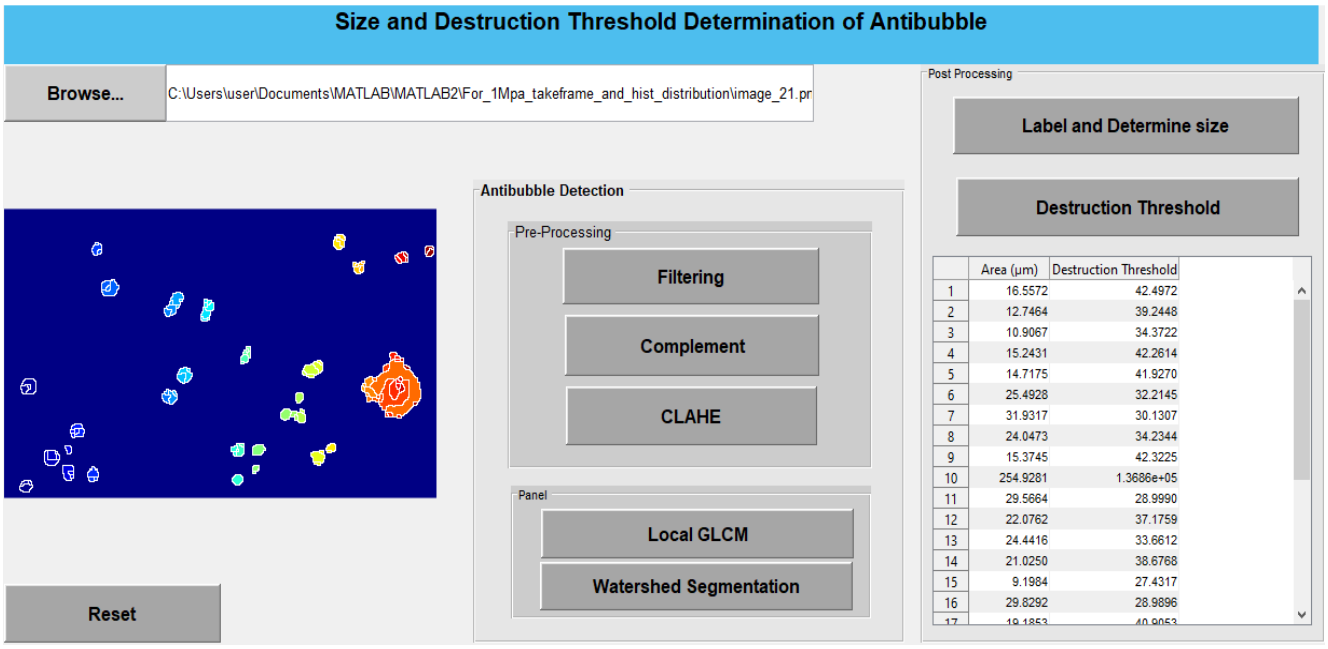

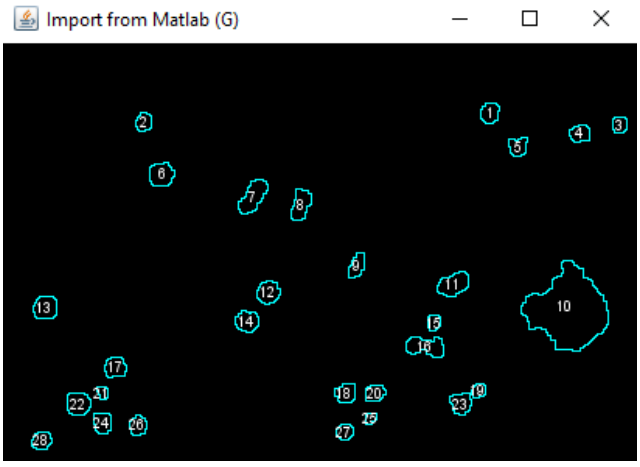

Appendix II: GLCM Features

Contrast

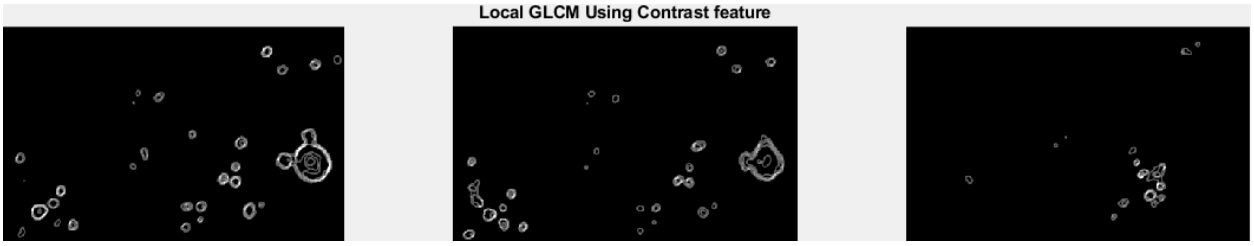

Correlation

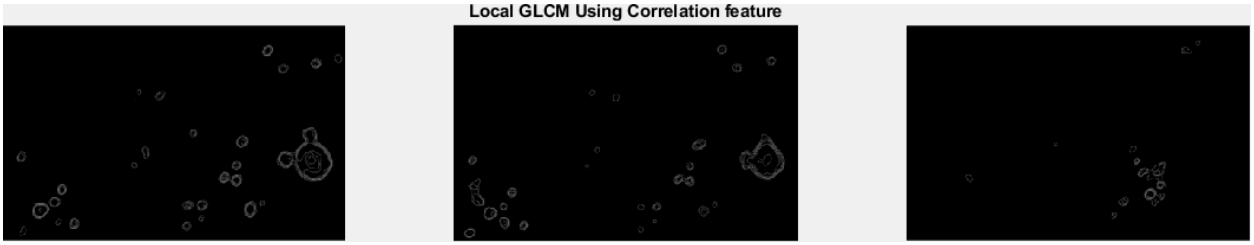

Homogeneity

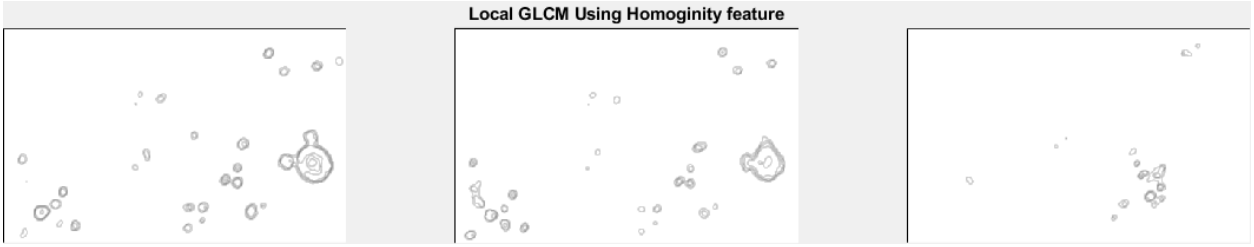

Energy

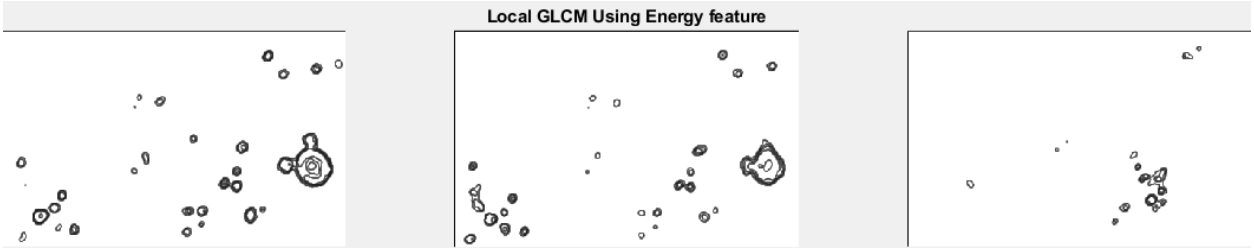

Entropy

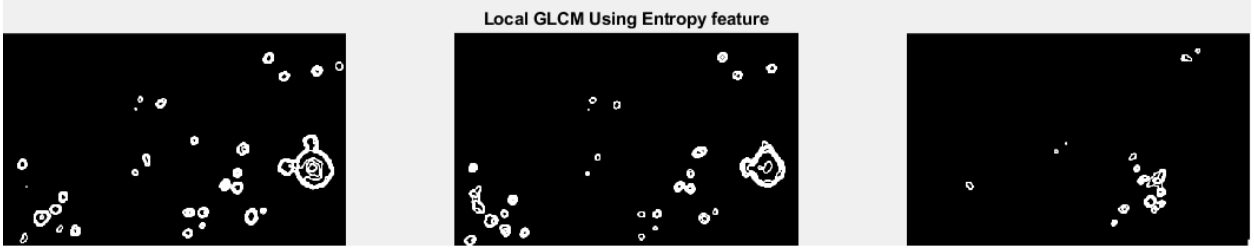

Cluster Prominence

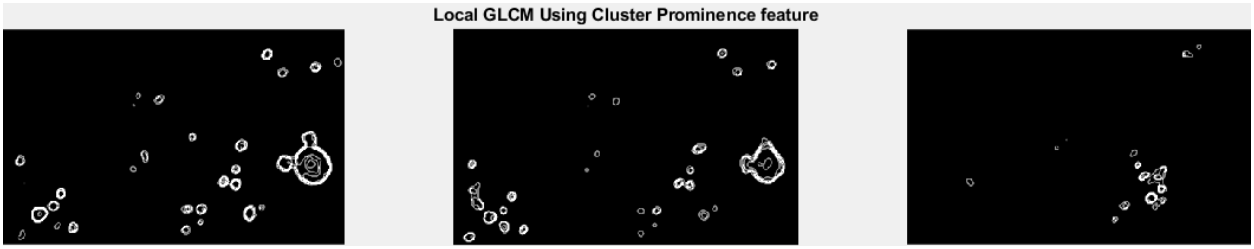

Cluster Shade

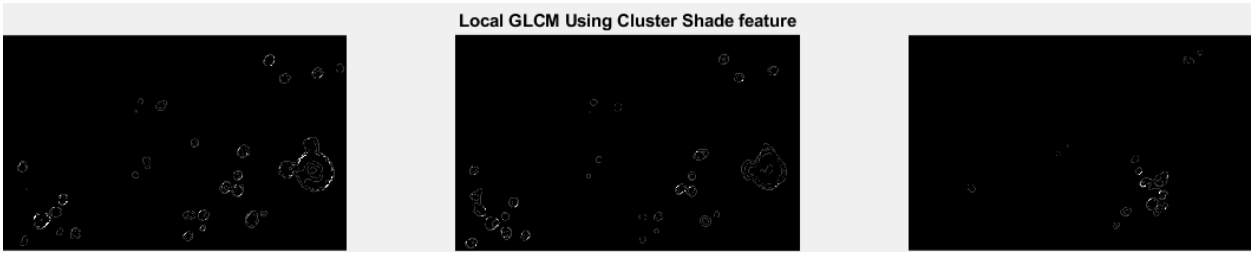

Dissimilarity

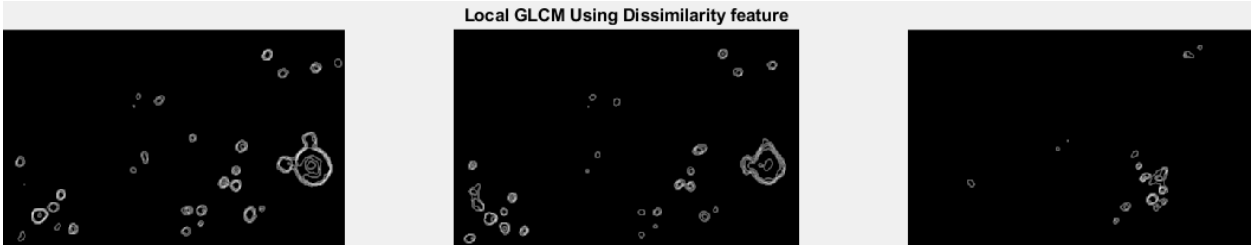

Maximum Probability

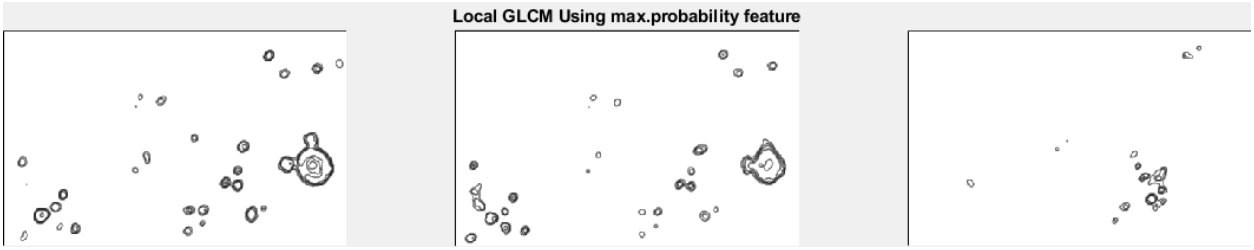

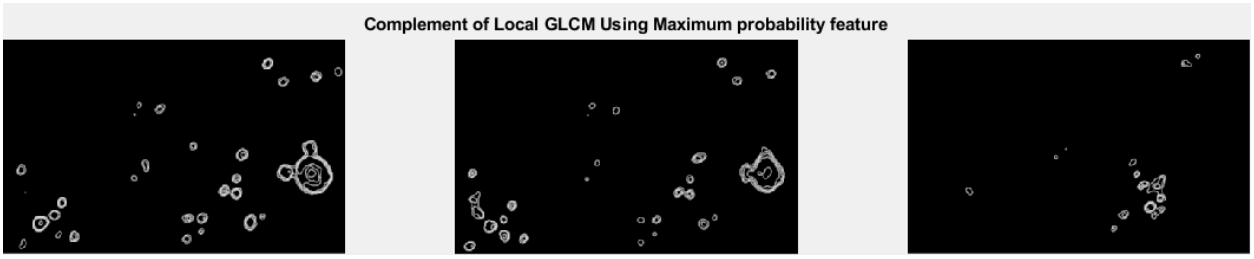

Appendix III: Size Distribution Analysis of Antibubbles under low Acoustic Pressures

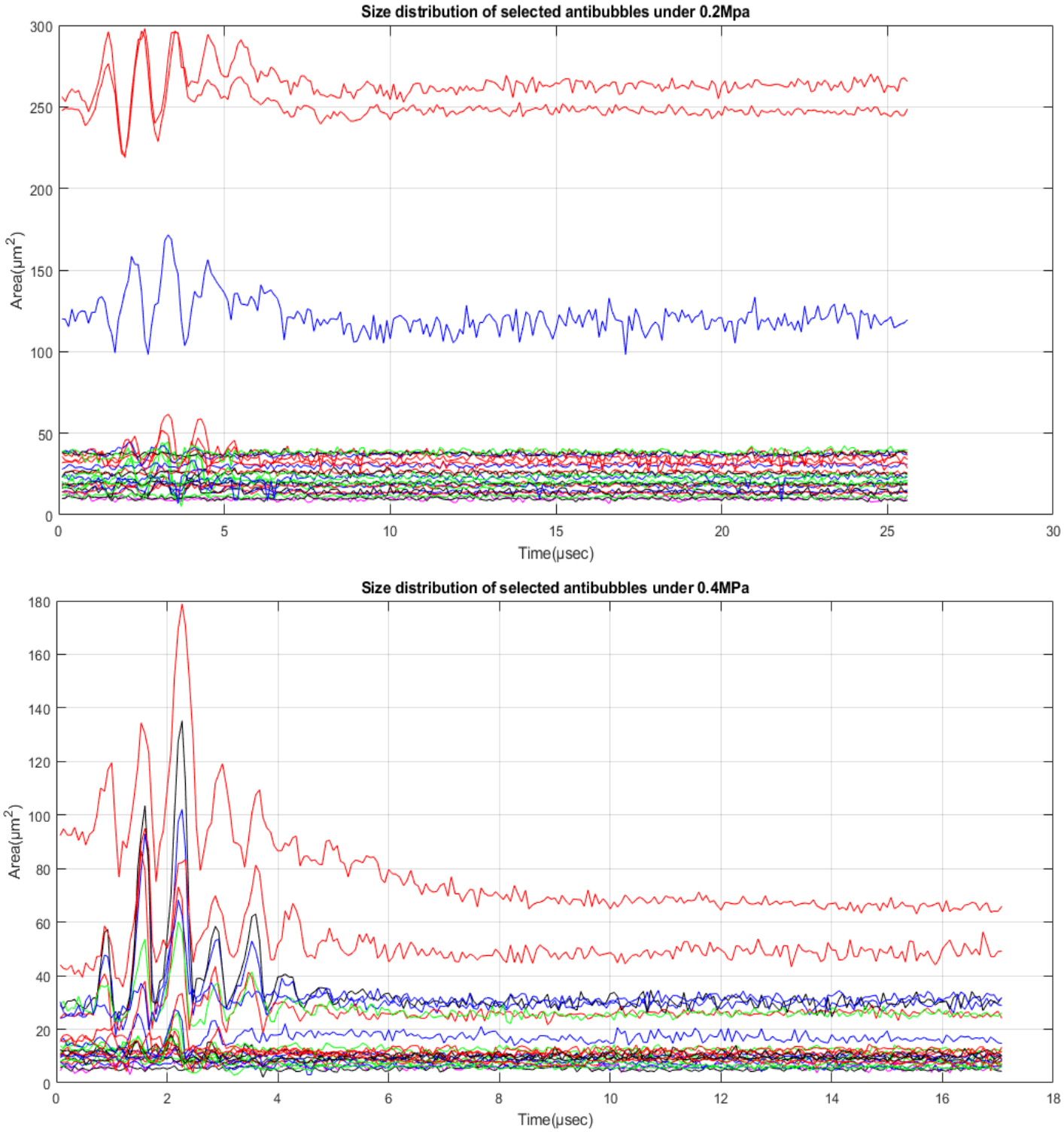

Figure III.1 Area time curve of selected antibubbles under low acoustic pressures, for 0.2 MPa (top), for 0.4 MPa (bottom).

Appendix IV: Destruction Threshold Analysis

No	0.6 MPa (PNP)				1 MPa (PNP)			
1.	Area(initial)	Area(max)	Ro	Rmax	Area(initial)	Area(max)	R0	Rmax
2.	6.702	17.346	1.46	2.35	1.577	2.628	0.71	0.91
3.	6.965	12.878	1.49	2.03	5.125	8.016	1.28	1.60
4.	7.395	15.637	1.53	2.23	7.753	14.98	1.57	2.18
5.	10.644	26.675	1.84	2.91	8.673	15.243	1.66	2.20
6.	10.907	18.971	1.86	2.46	8.936	32.195	1.69	3.20
7.	11.827	18.003	1.94	2.39	9.198	25.23	1.71	2.83
8.	12.352	32.063	1.98	3.20	12.089	21.156	1.96	2.60
9.	12.62	35.48	2.00	3.36	12.484	25.756	1.99	2.86
10.	13.27	26.413	2.06	2.90	12.746	25.624	2.01	2.86
11.	13.93	38.108	2.11	3.48	13.535	26.544	2.08	2.91
12.	14.46	28.515	2.15	3.01	14.455	60.053	2.15	4.37
13.	18.134	45.335	2.40	3.80	16.557	64.258	2.30	4.52
14.	19.771	43.233	2.51	3.71	16.689	42.707	2.31	3.69
15.	19.842	40.079	2.51	3.57	17.608	48.489	2.37	3.93
16.	20.499	50.591	2.56	4.01	18.528	54.928	2.43	4.18
17.	21.025	57.687	2.59	4.29	21.419	75.559	2.61	4.91
18.	21.419	47.438	2.61	3.89	21.945	65.703	2.64	4.57
19.	22.208	54.139	2.66	4.15	22.208	67.017	2.66	4.62
20.	23.39	51.774	2.73	4.06	23.653	58.607	2.74	4.32
21.	26.281	66.754	2.89	4.61	23.916	81.472	2.76	5.09
22.	26.413	59.133	2.90	4.34	24.836	124.705	2.81	6.30
23.	27.332	62.681	2.95	4.47	28.515	95.795	3.01	5.52
24.	33.114	74.376	3.25	4.87	36.137	117.083	3.39	6.11
25.	34.166	74.376	3.30	4.87	40.079	83.706	3.57	5.16
26.	37.976	86.334	3.48	5.24	41.13	72.536	3.62	4.81
27.	38.765	89.225	3.51	5.33	43.364	125.887	3.72	6.33
28.	50.986	109.067	4.03	5.89	43.364	126.544	3.72	6.35
29.	56.373	116.032	4.24	6.08	-	-	-	-

Table IV.1 Antibubble expansion relative to their initial size interms of area and radius during exposure to ultrasound witha peak negative pressure of 0.6 Mpa and 1MPa.